Originally published as:

Separation of local and regional information in distorted GDS response functions by hypothetical event analysis

Patricia Ritter* and Roger J. Banks

Department of Geology & Geophysics, Grant Institute, University of Edinburgh, Edinburgh, EH9 3JW, UK

SUMMARY

Electromagnetic investigations are usually intended to examine regional structures where induction takes place at a given period range. However, the regional information is often distorted by galvanic effects at local conductivity boundaries. Bahr (1985) and Groom & Bailey (1989) developed a physical distortion model for decomposing the MT impedance tensor, based upon local galvanic distortion of a regional 2-D electromagnetic field. We have extended their method to predict the magnetic variation fields created at an array of sites. The magnetic response functions at periods around 1000 s may be distorted by large-scale inhomogeneities in the upper or middle crust. In this period range, the data measured by a magnetometer array contain common information that can be extracted if the data set is treated as a unit, for example by using hypothetical event analysis. With this technique it is always possible to recover the regional strike direction from distorted data, even if a strong, spatially varying regional vertical field component is present in the data set. The determination of the regional impedance phases, on the other hand, is far more sensitive to deviations from the physical distortion model.

The approach has been used to investigate the Iapetus data set. For the array, which covers an area of 200 km × 300 km in northern England/southern Scotland, the technique revealed a common regional strike azimuth of *ca*. N125°E in the period range 500–2000 s. This direction differs from the strike indicated by the induction arrows, which seem influenced mainly by local current concentrations along the east–west-striking Northumberland Trough and a NE–SW-striking mid-crustal conductor. Both impedance phases are positive and differ by *ca*. 10°, which supports the assumptions of distortion fields in the data set and that the regional structure is 2-D.

Key words: channelled currents, electromagnetic induction, magnetovariation.

1 INTRODUCTION

Magnetotelluric (MT) and Geomagnetic Deep Sounding (GDS) surveys are usually applied to examine *regional* structures, where induction takes place at a given period range. However, it is a well-known difficulty that galvanic effects due to near-surface inhomogeneities can modify the regional MT impedance tensor and the magnetic response function in such a way that a 2-D interpretation becomes misleading (e.g. Jones 1983). The term galvanic distortion is usually employed for non-inductive processes at *local* structures, which are typically too small or too shallow to be involved in the induction process at the relevant period range. Instead, they are responsible for the deflection of regional currents induced in much larger,

deeper or more remote structures. This effect is thought to be caused by electrostatic fields due to surface charges on the local boundaries. The important factor determining the relative importance of distortion and induction is the ratio of the scale length of the local anomaly to the skin depth of the host material at the investigated period (see Fig. 1).

The effect of distortion on the electric field is frequency-independent, causing shift and rotation of the MT impedances at long periods. Several techniques to eliminate electric distortion have been developed in recent years; some of these are based on purely mathematical approaches, while others are based upon a physical model of distortion. Physical decomposition methods (Zhang *et al.* 1987; Bahr 1988; Groom & Bailey 1989) are now applied widely as almost standard procedures in MT interpretations. The spatial deflection of regional currents, however, also generates a local anomalous magnetic field that is superimposed on the regional magnetic field. As a consequence, distortion of the vertical magnetic

* Now at: GeoForschungsZentrum Potsdam, Telegrafenberg, D-14473 Potsdam, Germany. E-mail: pritter@gfz-potsdam.de
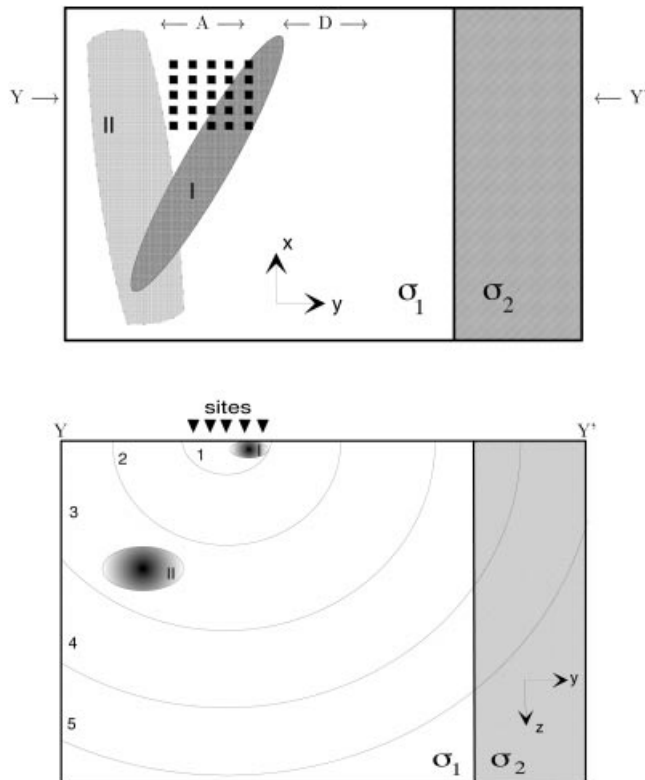
Figure 1. Schematic of induction and distortion processes in plan view and section. Upper figure (plan view): a sensor array located near two local structures (I and II) of limited horizontal extent. The large-scale regional structure is represented by the vertical boundary between two quarter-spaces with $\sigma_1 < \sigma_2$. Lower figure (vertical section along the profile YY'): vertical position of the two conductive inhomogeneities with respect to the skin depth of the electromagnetic field at five increasing periods. (1) At the shortest period, the shallow body (I) responds inductively. (2) Body I causes distortion of the regional 1-D response. (3) Induction in the mid-crustal body II; the electric field may still be distorted by currents channelled through body I. (4) Body II causes distortion of the regional 2-D response at long periods. (5) Distortion effects on the magnetic field may have already vanished, while electric distortion is still present in the MT response functions at very long periods.

response functions in GDS must also be considered. Its effects on single GDS sites and on the MT impedances have been examined recently with respect to decomposition methods by Zhang *et al.* (1993, 1995), Chave & Smith (1994) and Smith (1997).

Magnetic distortion—as opposed to electric distortion—is frequency-dependent because it is closely coupled to the regional impedance. Since its effects fall off with increasing period, it has been argued that data in the MT and especially the GDS period ranges are not affected (Zhang *et al.* 1987; Groom & Bailey 1989). This argument is based on the assumption that galvanic distortion is produced only by very small-scale, near-surface structures. Groom & Bailey (1991), for example, examine the effects of a conductive hemisphere that is located at the surface and has a radius of just 100 m. As a consequence, magnetic distortion appears in the short period range at $T < 10^{-2}$ s and is irrelevant at longer periods. However, at periods >100 s, upper- and mid-crustal structures with an extent of 10 km or more are smaller than the skin

depth and the major influence in this period range may take the form of scattering rather than induction (Chave & Smith 1994). Thus, conductivity anomalies of different scales may be responsible for a sequence of induction and distortion effects in different period ranges (Zhang *et al.* 1993).

Magnetic response functions are usually presented as induction arrows. However, in the period range where distortion dominates, their lengths and azimuths may be controlled entirely by the anomalous magnetic field of locally deflected regional currents. Nevertheless, the response functions also contain information about the regional geology. This information is common to all sites in a certain area depending on the period range. Hence the magnetic distortion problem can be formulated as a combination of site-dependent distortion parameters and contributions from site-independent regional induction processes. Zhang *et al.* (1993, 1995) and Chave & Smith (1994) proposed techniques for the elimination of magnetic distortion that use the MT impedances and are based on the analysis of observations at single sites.

In contrast to these single-site investigations, it is the purpose of this study to use the data from a spatially distributed array of GDS sites in order to extract the common regional information. Hypothetical event analysis (HEA) of magnetometer array data treats the data set as a unit, and therefore provides a very effective way of recovering such common information. If the results from HEA are presented in Argand diagrams, the regional and site-dependent parts of the vertical magnetic field can be separated without the need for complex inversion techniques. We show in Section 2.2 that with HEA it is possible to determine the regional strike direction and the regional impedance phases from distorted magnetic response functions.

In Section 3, we apply the method to real data. The Iapetus data set is a good example of an array where magnetic distortion is suspected. It comprises vertical magnetic response functions in the period range 10–7000 s from relatively densely spaced sites (10–20 km) in northern England and southern Scotland. The data are clearly influenced by current concentrations associated with the Northumberland Trough, causing strong anomalous vertical fields. Hypothetical event analysis, however, reveals that the data at these periods contain additional information that is common to all sites. This common information suggests a different strike azimuth that we conclude is the strike direction of the regional structure.

A further application of this technique to measured data can be found in Ritter & Ritter (1997), where an analysis of the magnetic response functions from British Columbia (BC87 data set) is performed successfully, despite the fact that for this region the assumptions made for the basic distortion model are not met exactly.

2 THEORETICAL BACKGROUND

2.1 Magnetic distortion model

Electric and magnetic distortion effects are caused by the spatial deviations of uniform regional currents through or around a local anomaly, depending on the resistivity contrast to the host material. The local anomaly is generally assumed to be (much) smaller than the skin depth of the investigated period range in the host. The effects on the regional electric field $\mathbf{E}^o$ are commonly expressed by the electric distortion

tensor C, which consists of four real, frequency-independent components. The measured electric field is then $\mathbf{E} = C\mathbf{E}^{\mathrm{o}}$ (Zhang *et al.* 1987). Similarly, magnetic distortion can be represented by a real tensor D that acts on the regional electric field. The anomalous magnetic field $\mathbf{B}^{\mathrm{a}}$ generated by this process is *in phase* with the regional electric field and can be expressed by

$$\mathbf{B}^{\mathrm{a}} = D \cdot \mathbf{E}^{\mathrm{o}} \implies \varphi(\mathbf{B}^{\mathrm{a}}) = \varphi(\mathbf{E}^{\mathrm{o}}). \tag{1}$$

The magnetic distortion matrix D consists of six real, frequency-independent parameters (Zhang *et al.* 1987), two of which are used to describe the effects on the vertical field. The regional electric field $\mathbf{E}^{\mathrm{o}}$ in eq. (1) can now be replaced by the product of the regional MT impedance tensor Z^{o} and the horizontal magnetic field $\mathbf{B}^{\mathrm{o}}$:

$$\mathbf{B}^{\mathrm{a}} = DZ^{\mathrm{o}} \cdot \mathbf{B}^{\mathrm{o}}. \tag{2}$$

This substitution is based on the assumption that the regional fields are uniform, which implies that the local anomaly is sufficiently removed either horizontally or vertically from the regional lateral conductivity boundaries. In particular, the regional vertical magnetic field B_z^{o} is assumed to be spatially uniform over the area of interest (e.g. across the sensor array in area A in Fig. 1), and possibly small or of zero magnitude. This means that the spatial variation of the observed vertical component is due to local distortion only ($B_z - B_z^{\mathrm{o}} = B_z^{\mathrm{a}}$). It follows that the phase shift between the anomalous and the regional magnetic fields is equal to the phase of the regional impedance: $\varphi(\mathbf{B}^{\mathrm{a}}, \mathbf{B}^{\mathrm{o}}) = \varphi(Z^{\mathrm{o}})$.

Fig. 1 is a schematic representation of the response of a multiscale structure to an electromagnetic field. The contributions from induction and distortion processes to the observed fields strongly depend on the ratio of the length scale L of an inhomogeneity to the skin depth δ of the investigated period range.

For the vertical component of the anomalous magnetic field, eq. (2) contains two magnetic distortion parameters:

$$B_z^{\mathrm{a}} = (D_{zx}, D_{zy})Z^{\mathrm{o}}\begin{pmatrix} B_x^{\mathrm{o}} \\ B_y^{\mathrm{o}} \end{pmatrix}. \tag{3}$$

This expression is similar to the definition of the magnetic response function for 2-D induction: $B_z = (\mathscr{A}, \mathscr{B})\mathbf{B}$ (e.g. Hobbs 1992), which relates the measured vertical to the horizontal magnetic field. Even in the absence of a regional vertical component (e.g. above a conductive area), the magnetic response function may exist, created by the local distortion of the electromagnetic fields. The information on the regional structure is then contained in the impedance tensor Z^{o}:

$$(\mathscr{A}, \mathscr{B}) = (\mathscr{A}^{\ell}, \mathscr{B}^{\ell}) = (D_{zx}, D_{zy})Z^{\mathrm{o}}. \tag{4}$$

Hence we call $(\mathscr{A}^{\ell}, \mathscr{B}^{\ell})$ the local magnetic response function. Since the distortion parameters are real quantities, it is clear that the phase information contained in the local response function is solely related to the regional MT impedance tensor. The regional phase information must be contained in all response functions of a whole array of sites at a given period, if all these sites represent the same regional geology.

For the application of the above equations to real data a certain deviation from the theoretical model must be admitted, as the observed field $\mathbf{B}$ contains the regional magnetic field as well as the local anomalous field: $\mathbf{B} = \mathbf{B}^{\mathrm{o}} + \mathbf{B}^{\mathrm{a}}$. Ideally, the

difference field transfer functions should be used to reduce the influence of the anomalous horizontal fields. In view of the application of HEA described in Section 2.2, lateral variations of less than 30 per cent may be acceptable (Bailey *et al.* 1974), if only single-site transfer functions are available.

Suppose the local heterogeneity is embedded in a 1-D earth and is elongated in the x''-direction at an angle θ_{ℓ} to the measurement coordinates. It can then be regarded as locally approximating a 2-D structure that can be described by two parameters, D_{zx}'' and θ_{ℓ}. The vertical field is generated by the electrical field component in the strike direction $E_x^{\mathrm{o}''}$:

$$B_z^{\mathrm{a}} = (D_{zx}'', 0)\begin{pmatrix} E_x^{\mathrm{o}''} \\ E_y^{\mathrm{o}''} \end{pmatrix}, \tag{5}$$

where double-primed quantities are measured in local strike coordinates (x'', y''). In observation coordinates (x, y), this expression yields[1]:

$$B_z^{\mathrm{a}} = (D_{zx}'', 0)R_{\theta_{\ell}}^{\mathrm{T}}Z^{\mathrm{o}}\begin{pmatrix} B_x^{\mathrm{o}} \\ B_y^{\mathrm{o}} \end{pmatrix}.$$

For the local magnetic response function (eq. 4) we obtain

$$(\mathscr{A}^{\ell}, \mathscr{B}^{\ell}) = (D_{zx}'' \cos \theta_{\ell}, D_{zx}'' \sin \theta_{\ell})Z^{\mathrm{o}}.$$

It follows that, for a local 2-D anomaly, the magnetic distortion parameters in observation coordinates may be defined as

$$(D_{zx}, D_{zy}) = (D_{zx}'' \cos \theta_{\ell}, D_{zx}'' \sin \theta_{\ell}). \tag{6}$$

They are functions of position and of the geometry of the anomaly. D_{zx}'' varies as the observation point is moved relative to the body. The local strike may vary if the anomaly is not exactly 2-D. Local strike directions then also depend on the relative position of the observation point.

In the following sections the influence of distortion on the magnetic response function will be investigated for 1-D and 2-D regional conductivity distributions.

2.1.1 Distortion effects for a 1-D regional model

The MT impedance tensor for a 1-D conductivity distribution ($\sigma = \sigma(z)$) takes the form

$$Z^{\mathrm{o}} = \begin{pmatrix} 0 & Z \\ -Z & 0 \end{pmatrix}. \tag{7}$$

As there exists no regional vertical component for the 1-D case ($B_z^{\mathrm{o}} = 0$), the measured field contains only the anomalous, local field ($B_z = B_z^{\mathrm{a}}$). Eq. (3) then becomes

$$B_z = \underbrace{-D_{zy}Z}_{\mathscr{A}^{\ell}} B_x^{\mathrm{o}} + \underbrace{D_{zx}Z}_{\mathscr{B}^{\ell}} B_y^{\mathrm{o}}, \tag{8}$$

with

$$\mathscr{A}^{\ell} = -D_{zx}'' Z \sin \theta_{\ell},$$

$$\mathscr{B}^{\ell} = D_{zx}'' Z \cos \theta_{\ell}. \tag{9}$$

---

[1] Rotation matrix for angle θ: $R_{\theta} = \begin{pmatrix} \cos \theta & -\sin \theta \\ \sin \theta & \cos \theta \end{pmatrix}$; $R_{\theta}^{\mathrm{T}} = \begin{pmatrix} \cos \theta & \sin \theta \\ -\sin \theta & \cos \theta \end{pmatrix}$.

The components of the local magnetic response function $\mathscr{A}^\ell$ and $\mathscr{B}^\ell$ differ only by real, frequency-independent parameters. This observation leads to the following conclusions.

Phase. Both components contain the same 1-D impedance and therefore the same phase information:

$$\varphi(\mathscr{A}_i^\ell) = \varphi(\mathscr{B}_i^\ell) = \varphi(Z) . \tag{10}$$

This phase information must be the same at all sites (index i) representing the same regional geology. Consequently, in the complex plane, the real and imaginary parts of all $\mathscr{A}_i$ and $\mathscr{B}_i$ values at a given period will fall on a line through the origin. The gradient of this line indicates the regional impedance phase angle at that period (Figs 2a and b).

Variation with period. Another consequence of the fact that $\mathscr{A}^\ell(T)$ and $\mathscr{B}^\ell(T)$ differ only by real parameters is that the components (i.e. their logarithms) show the same period dependency; their ratio is

$$\frac{\mathscr{A}_i^\ell(T)}{\mathscr{B}_i^\ell(T)} = -\tan\theta_{\ell_i} . \tag{11}$$

The curves of the components at all sites are determined entirely by the 1-D impedance $Z(T)$; they are scaled by the magnetic distortion parameters. The ratios of the components at different sites, e.g. $\mathscr{A}_i$ and $\mathscr{A}_j$, will be independent of frequency over the period range where magnetic distortion occurs (see Fig. 2e).

Induction arrows. The direction Θ of induction arrows is calculated from the ratio of the two components of the magnetic response function (Wiese convention). For a 1-D regional conductivity distribution, induction arrows do not exist, because the vertical component is zero. In the presence of galvanic distortion, however, real and imaginary arrows (**P, Q**) can be computed. They point perpendicular to the strike direction of the local anomaly:

$$\theta_{P,Q} = \arctan\frac{\mathscr{R}e\,\mathscr{B}^\ell}{\mathscr{R}e\,\mathscr{A}^\ell} = \arctan\frac{\mathscr{I}m\,\mathscr{B}^\ell}{\mathscr{I}m\,\mathscr{A}^\ell} = \arctan\frac{\cos\theta_\ell}{-\sin\theta_\ell}$$

$$= \theta_\ell - 90° . \tag{12}$$

Over the period range of distortion, this direction is constant for all sites located along the long axis of the same local anomaly. Sites positioned at the ends of an elongated anomaly will show directions depending on the particular form of the body. The lengths of the arrows vary according to the frequency dependence of the real and imaginary parts of Z and according to their position. For example, sites located directly above a conducting body will have smaller arrows than those above the resistive host:

real arrow: $L_P = \sqrt{(\mathscr{R}e\,\mathscr{A}^\ell)^2 + (\mathscr{R}e\,\mathscr{B}^\ell)^2}$

$$= |D_{zx}''(\mathbf{r})\mathscr{R}e\,Z(T)| ;$$

imaginary arrow: $L_Q = \sqrt{(\mathscr{I}m\,\mathscr{A}^\ell)^2 + (\mathscr{I}m\,\mathscr{B}^\ell)^2}$

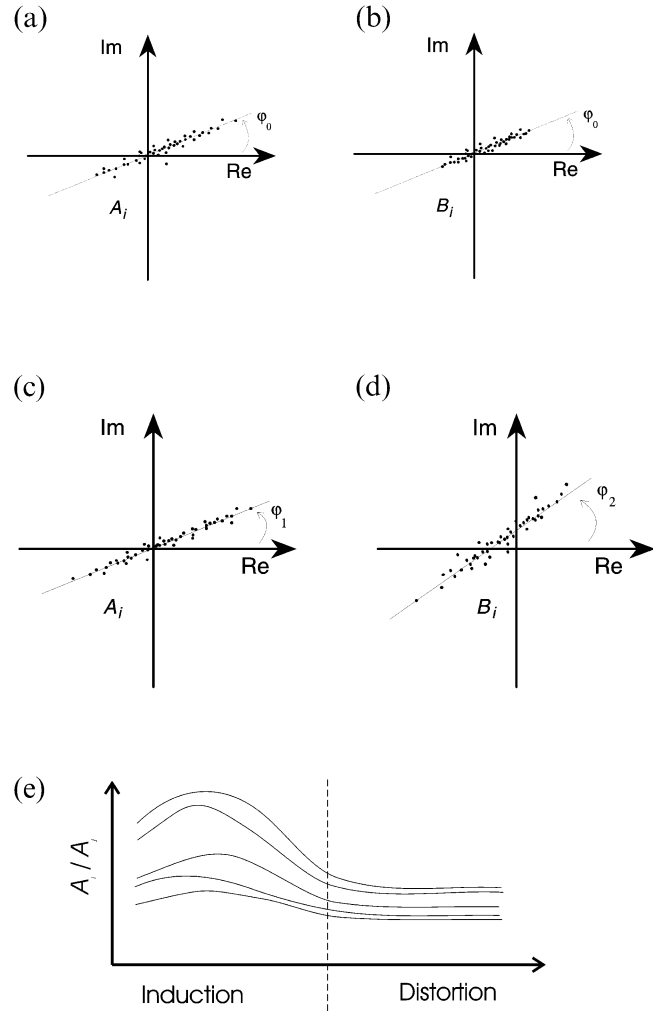$$= |D_{zx}''(\mathbf{r})\mathscr{I}m\,Z(T)| . \tag{13}$$

Figure 2. Behaviour of the distorted magnetic response functions ($\mathscr{A}$, $\mathscr{B}$). (a), (b) 1-D regional structure: Argand diagrams of $\mathscr{A}$ and $\mathscr{B}$ at one period. The same phase φ_o is exhibited by all sites in both $\mathscr{A}$ and $\mathscr{B}$. (c), (d) 2-D regional structure: the components display different phases as they contain different impedances, $\varphi_1(Z_B)$ and $\varphi_2(Z_E)$. The line indicated for $\mathscr{B}_i$ is shifted away from the origin due to a superimposed regional vertical magnetic field. (e) 1-D or 2-D regional structure: ratios $\mathscr{A}_i(T)/\mathscr{A}_j(T)$ at five different sites.

Length variations between sites depend only on the parameters of position $D_{zx}''(\mathbf{r}_i)$. The relative lengths of the real and imaginary arrows depend on the variation of conductivity with depth:

(1) homogeneous half-space: phase: $\varphi(Z) = 45°$; $L_P = L_Q$;
(2) resistor at depth: phase: $\varphi(Z) < 45°$; $L_P > L_Q$;
(3) conductor at depth: phase: $\varphi(Z) > 45°$; $L_P < L_Q$.

2.1.2   Distortion effects for a 2-D regional model

For a 2-D conductivity distribution ($\sigma = \sigma(x', z)$), the MT impedance tensor in the coordinate system (x', y') of the regional strike θ_r takes the form

$$Z^\circ = \begin{pmatrix} 0 & Z_E \\ Z_B & 0 \end{pmatrix} . \tag{14}$$

Consequently, we obtain for the vertical anomalous magnetic field component (eq. 3) the following expression:

$$B_z^a = \underbrace{D'_{zy} Z_B}_{\mathscr{A}^{\ell'}} B_x^{o'} + \underbrace{D'_{zx} Z_E}_{\mathscr{B}^{\ell'}} B_y^{o'} . \qquad (15)$$

The total magnetic response function may include contributions from a regional vertical component B_z^o and therefore it may contain the additional term $\mathscr{B}^{o'}$ ($\mathscr{A}^{o'} = 0$ in x', y'!):

$$(\mathscr{A}', \mathscr{B}') = [(0, \mathscr{B}^{o'}) + (D''_{zx}, 0)\boldsymbol{R}_\alpha^T \boldsymbol{Z}^o] ; \qquad (16)$$

hence

$$\mathscr{A}' = D''_{zx} Z_B \sin \alpha , \qquad (17)$$

$$\mathscr{B}' = D''_{zx} Z_E \cos \alpha + \mathscr{B}^{o'} . \qquad (18)$$

As before, double primes denote local coordinates (x'', y''). α is the local strike direction relative to the regional coordinate system. The fact that, when expressed in regional strike coordinates, each of the local response function components contains only one of the principal impedances has the following consequences for the phase and frequency dependences.

Phase. The phases of $\mathscr{A}_i^{\ell'}$ and $\mathscr{B}_i^{\ell'}$ are solely determined by the phase of one principal impedance, Z_B and Z_E, respectively. All sites representing the same regional geology will produce the same phases for the local response function components at a given period, regardless of position and local strike direction (Figs 2c and d):

$$\varphi(\mathscr{A}_i^{\ell'}) = \varphi(Z_B) \quad \text{and} \quad \varphi(\mathscr{B}_i^{\ell'}) = \varphi(Z_E) \quad \text{if} \quad B_z^o = 0 . \qquad (19)$$

If the components $\mathscr{A}_i'$ and $\mathscr{B}_i'$ are displayed in Argand diagrams (i.e. in the complex plane), they will fall on lines indicating the regional impedance phases of Z_B and Z_E, respectively. If a spatially uniform, regional vertical component B_z^o exists, the phase for components $\mathscr{B}'$ will be shifted by $\mathscr{B}^{o'}$. However, since the values at every site are shifted by the same amount, the inclination of the phase line is not affected and it indicates the correct impedance phase angle. Only if the regional magnetic field is non-uniform, because the sites are located close to the regional structure, will the distribution of $\mathscr{B}_i'$ in the Argand diagrams become less linear. Component $\mathscr{A}'$ is not affected, because the regional contribution $\mathscr{A}^{o'}$ equals zero for a strike direction along x'.

Variation with period. As the components $\mathscr{A}^{\ell'}(T)$ and $\mathscr{B}^{\ell'}(T)$ each contain only one of the principal impedances, their frequency response curves are determined by either Z_E or Z_B. For that reason, the curves of $\mathscr{A}'$ and $\mathscr{B}'$ at any one site are shaped differently. The ratio of the $\mathscr{A}$-response at any one site to that at any other will be independent of period over the period range of magnetic distortion. Fig. 2(e) is again appropriate. However, the regional field reflects a frequency-dependent induction process, and its changing contribution will cause the $\mathscr{B}$-ratios to vary.

Induction arrows. With eq. (17), the direction of the induction arrows is determined by the ratio of the two principal impedances, the relative local strike θ_α and, if present, the regional vertical field B_z^o:

$$\theta_{P,Q} = \arctan\left(\frac{\mathscr{B}_i'}{\mathscr{A}_i'}\right) = \arctan\left(\frac{Z_E \cos \alpha_i + \mathscr{B}^{o'}}{Z_B \sin \alpha_i}\right) . \qquad (20)$$

For the real and imaginary arrows (**P** and **Q**), the real and imaginary parts of the principal impedances and $\mathscr{B}^{o'}$ apply. The presence of a spatially uniform regional component B_z^o affects the arrows considerably but equally at all sites:

$$L_P = \sqrt{D''^2_{zx}((\mathscr{Re}\, Z_E)^2 + (\mathscr{Re}\, Z_B)^2) + (\mathscr{Re}\, \mathscr{B}^{o'})^2} ,$$

$$L_Q = \sqrt{D''^2_{zx}((\mathscr{Im}\, Z_E)^2 + (\mathscr{Im}\, Z_B)^2) + (\mathscr{Im}\, \mathscr{B}^{o'})^2} . \qquad (21)$$

Lengths L_P and L_Q at different sites vary only depending on the parameter of position $D''_{zx}(\mathbf{r}_i)$ or on a spatially non-uniform $\mathscr{B}^{o'}$, if applicable.

In *measurement coordinates*, the equation for the vertical anomalous magnetic field component (eq. 3) also contains rotational terms:

$$B_z^a = (D_{zx}, D_{zy})\boldsymbol{R}_{\theta_r} \begin{pmatrix} 0 & Z_E \\ Z_B & 0 \end{pmatrix} \boldsymbol{R}_{\theta_r}^T \begin{pmatrix} B_x^o \\ B_y^o \end{pmatrix}$$

$$= \mathscr{A}^\ell B_x^o + \mathscr{B}^\ell B_y^o . \qquad (22)$$

Using the local magnetic distortion parameters, eq. (22) becomes

$$B_z^a = (D''_{zx}, 0)\boldsymbol{R}_{\theta_\ell}^T \boldsymbol{R}_{\theta_r} \boldsymbol{Z}^o \boldsymbol{R}_{\theta_r}^T \mathbf{B}^o$$

$$= (D''_{zx}, 0)\boldsymbol{R}_\alpha^T \boldsymbol{Z}^o \boldsymbol{R}_{\theta_r}^T \mathbf{B}^o , \quad \text{with } \alpha = \theta_\ell - \theta_r . \qquad (23)$$

The observation coordinates (x, y) are in the north and east directions at ($0°$, $90°$), respectively. θ_r and θ_ℓ are the regional and local strike directions with respect to the observation coordinates (x). With this notation, we obtain the following expressions for the components of the local magnetic response function:

$$\mathscr{A}^\ell = D''_{zx} \cdot [-Z_E \sin \theta_r \cos \alpha + Z_B \cos \theta_r \sin \alpha] , \qquad (24a)$$

$$\mathscr{B}^\ell = D''_{zx} \cdot [Z_E \cos \theta_r \cos \alpha + Z_B \sin \theta_r \sin \alpha] . \qquad (24b)$$

Both components contain mixtures of the two principal impedances and of the local and regional strike directions. The interpretation of phase behaviour, variation with period and orientation of induction arrows is therefore difficult, especially if the regional vertical component B_z^o is non-zero. In this case, the regional response function ($\mathscr{A}^o$, $\mathscr{B}^o$) is added to the local response function:

$$B_z = B_z^o + B_z^a = (\mathscr{A}, B)\mathbf{B}^o$$

$$= [(\mathscr{A}^o, \mathscr{B}^o) + (\mathscr{A}^\ell, \mathscr{B}^\ell)]\mathbf{B}^o . \qquad (25)$$

Hence, the total magnetic response function becomes

$$(\mathscr{A}, \mathscr{B}) = [(0, \mathscr{B}^{o'})\boldsymbol{R}_{\theta_r}^T + (D''_{zx}, 0)\boldsymbol{R}_\alpha^T \boldsymbol{Z}^o \boldsymbol{R}_{\theta_r}^T] . \qquad (26)$$

2.2 Hypothetical event analysis

One way of representing the spatial information contained within a collection of magnetic response measurements is to make use of hypothetical event analysis. The aim is to try to simulate the vertical magnetic field (B_z^p) which would be observed at each measurement point when the regional horizontal magnetic field (assumed to be uniform over the area) has a specified amplitude (say 1 nT) and direction (ϑ^*). If response functions ($\mathscr{A}$, $\mathscr{B}$) have been determined that link the vertical

magnetic field at each site to the horizontal field at a reference site that is representative of the regional field, then the vertical field can be simulated directly:

$$B_z^p = (\mathscr{A}, \mathscr{B})\mathbf{B}_h^* = (\mathscr{A}, \mathscr{B}) \cdot \begin{pmatrix} 1 \cdot \cos \vartheta^* \\ 1 \cdot \sin \vartheta^* \end{pmatrix}. \qquad (27)$$

However, it is more usual for only single-station response functions to be available, linking the vertical magnetic field at each site to the horizontal field at the same site. Simulating the horizontal magnetic field at a site by a uniform value will be inaccurate because the single-site response functions contain the influence of anomalous horizontal fields. It may be argued that the anomalous horizontal fields are only a small fraction of the total—Banks & Beamish (1984) suggest <20 per cent, Bailey *et al.* (1974) 30 per cent—but it would still be preferable where possible to use interstation response functions. Banks (1986) showed how knowledge of the spatial structure of the vertical field, generated by HEA using single-station response functions, can be used to compute the anomalous horizontal fields and hence estimate the required interstation response. For the purposes of the theoretical analysis, we shall assume that the horizontal magnetic field at each site is the same. For practical applications, this means that, ideally, response functions measured relative to a common site should be available, either determined directly from simultaneous measurements, or estimated using procedures such as that proposed by Banks (1986).

2.2.1 Elimination of magnetic distortion

For the purpose of revealing regional information from distorted magnetic response functions, we investigate the expression for the predicted vertical field in the presence of magnetic distortion:

$$B_z^p = (\mathscr{A}, \mathscr{B})\mathbf{B}_h^* = [(\mathscr{A}^\circ, \mathscr{B}^\circ) + (D_{zx}, D_{zy})\mathbf{Z}^\circ] \begin{pmatrix} 1 \cdot \cos \vartheta^* \\ 1 \cdot \sin \vartheta^* \end{pmatrix}.$$

$$(28)$$

Obviously, if the hypothetical event is polarized in a northward or eastward direction and has zero phase, the predicted value B_z^p is simply the corresponding component of the magnetic response function:

$$B_z^p = \mathscr{A} \qquad \text{for} \quad \vartheta^* = 0^\circ, \qquad (29a)$$

$$B_z^p = \mathscr{B} \qquad \text{for} \quad \vartheta^* = 90^\circ. \qquad (29b)$$

In the following, the information content of the vertical field predicted using HEA will be investigated for regional 1-D and 2-D settings.

HEA for a regional 1-D model. For a regional 1-D conductivity distribution the expression in eq. (28) simplifies and for the predicted vertical field we obtain

$$B_z^p = -D_{zy}Z \cos \vartheta^* + D_{zx}Z \sin \vartheta^* \qquad (30)$$

$$= Z(D_{zx} \sin \vartheta^* - D_{zy} \cos \vartheta^*). $$

Because the distortion parameters D_{zx} and D_{zy} are real, the phase of B_z^p is the phase of the impedance Z. It follows that

the phases of the predicted values at all sites must be equal to the phase of the 1-D impedance, irrespective of the direction of the hypothetical event. If the real and imaginary parts of $B_{z_i}^p$ for all sites representing the same regional 1-D structure are plotted in an Argand diagram, they range along a line through the origin that indicates the regional 1-D phase. The slope of this line will be unaltered if the azimuth ϑ^* is changed. Again, Figs 2(a) and (b) can be taken as references, because for a unit amplitude of the hypothetical field, the predicted values $B_{z_i}^p$ at azimuths $\vartheta^* = 0^\circ$ and $\vartheta^* = 90^\circ$ equal the $\mathscr{A}$ and $\mathscr{B}$ components.

Inclusion of the local strike direction into eq. 30 shows that B_z^p must become very small if the azimuth ϑ^* approximates the local strike direction. If, on the other hand, a field direction perpendicular to the local structure is approached, the predicted value reaches a maximum:

$$B_z^p = -D_{zx}''Z \sin \theta_\ell \cos \vartheta^* + D_{zx}''Z \cos \theta_\ell \sin \vartheta^* \qquad (31)$$

$$= -D_{zx}''Z \sin (\theta_\ell - \vartheta^*);$$

hence

$$\begin{aligned} B_z^p &= 0 & \text{for} \quad \vartheta^* = \theta_\ell, \\ B_z^p &= D_{zx}''Z & \text{for} \quad \vartheta^* = \theta_\ell + 90^\circ. \end{aligned} \qquad (32)$$

In order to find the local strike, the data for all sites can be examined for minimum/maximum amplitudes in the Argand diagrams by gradually changing the direction of the magnetic field. A more straightforward way to determine the local strike is from the ratio of the predicted values for perpendicular field directions at each site:

$$\frac{B_{z_i}^p(0^\circ)}{B_{z_i}^p(90^\circ)} = \frac{\mathscr{A}_i^\ell}{\mathscr{B}_i^\ell} = -\tan \theta_{\ell_i}. \qquad (33)$$

θ_ℓ may also be determined graphically by plotting the real parts of the $B_{z_i}^p$ in an '$\mathscr{A}$ versus $\mathscr{B}$' diagram (see Fig. 3).

HEA for a regional 2-D model. For a 2-D regional structure, the predicted value for the vertical magnetic field contains the principal impedances and the regional strike. In observation
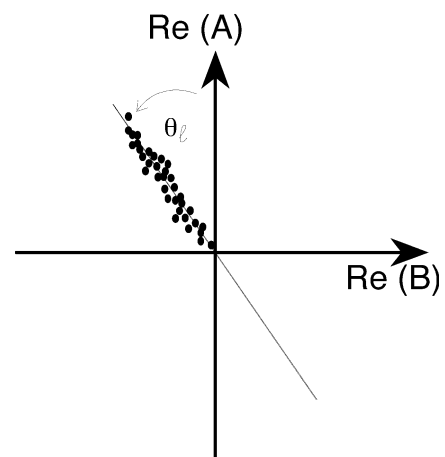

Figure 3. Schematic diagram of $\mathscr{A}$ versus $\mathscr{B}$ for a regional 1-D model. The predicted vertical fields $\mathscr{R}e\, B_{z_i}^p$ at perpendicular directions of the magnetic field (0° and 90°) form a line indicating the local strike azimuth θ_ℓ.

coordinates we obtain:

$$B_z^p = [(0, \mathscr{B}^{o'})\boldsymbol{R}_{\theta_r}^T + (\mathscr{A}^\ell, \mathscr{B}^\ell)\boldsymbol{R}_{\theta_r}^T]\boldsymbol{B}_h^* \qquad (34a)$$

$$= [(0, \mathscr{B}^{o'})\boldsymbol{R}_{\theta_r}^T + (D_{zx}, D_{xy})\boldsymbol{R}_{\theta_r}\boldsymbol{Z}^o\boldsymbol{R}_{\theta_r}^T]\begin{pmatrix} 1 \cdot \cos\vartheta^* \\ 1 \cdot \sin\vartheta^* \end{pmatrix}. \qquad (34b)$$

Explicitly, this general expression yields

$$B_z^p(\vartheta^*) = D_{zx} \cdot [Z_E \cos\theta_r \sin(\vartheta^* - \theta_r) - Z_B \sin\theta_r \cos(\vartheta^* - \theta_r)]$$

$$+ D_{zy} \cdot [Z_E \sin\theta_r \sin(\vartheta^* - \theta_r) + Z_B \cos\theta_r \cos(\vartheta^* - \theta_r)]$$

$$+ \mathscr{B}^{o'} \sin(\vartheta^* - \theta_r). \qquad (35)$$

For a perpendicular azimuth we obtain a similar expression:

$$B_z^p(\vartheta^* + 90°)$$

$$= D_{zx} \cdot [Z_E \cos\theta_r \cos(\vartheta^* - \theta_r) + Z_B \sin\theta_r \sin(\vartheta^* - \theta_r)]$$

$$+ D_{zy} \cdot [Z_E \sin\theta_r \cos(\vartheta^* - \theta_r) - Z_B \cos\theta_r \sin(\vartheta^* - \theta_r)]$$

$$+ \mathscr{B}^{o'} \cos(\vartheta^* - \theta_r). \qquad (36)$$

These equations simplify considerably for the special cases when ϑ^* is either parallel to the regional strike direction θ_r or perpendicular to it:

$$\vartheta^* = \theta_r: \ B_z^p = Z_B[-D_{zx}\sin\theta_r + D_{zy}\cos\theta_r],$$
$$\vartheta^* \perp \theta_r: \ B_z^p = Z_E[D_{zx}\cos\theta_r + D_{zy}\sin\theta_r] + \mathscr{B}^{o'}. \qquad (37)$$

Note that in both cases the predicted value contains only one of the principal impedances. If we include the local strike direction in the distortion parameters (using eq. 6), we find relations that are familiar from the previous section:

$$\vartheta^* = \theta_r: \qquad B_z^p = D_{zx}''Z_B\sin\alpha \qquad = \mathscr{A}',$$
$$\vartheta^* = \theta_r + 90°: \quad B_z^p = D_{zx}''Z_E\cos\alpha + \mathscr{B}^{o'} = \mathscr{B}'. \qquad (38)$$

In fact, the expressions for the predicted B_z^p are in these two cases the same as for the response function components in *regional strike coordinates* (eq. 17). Hence, the characteristics described in the previous section (2.1.2) can be used to recover the common regional strike azimuth from the observed data array. By gradually varying the direction ϑ^* of the magnetic field and monitoring the predicted vertical fields of all sites simultaneously (at one given period) using an Argand diagram, we can find the regional strike. It corresponds to the horizontal field azimuth for which the data points fall on a line through the origin. The gradient of this line indicates the phase angle of one of the regional impedances (Z_B).

If an azimuth perpendicular to the regional strike is selected, the values will scatter along the phase line of the orthogonal principal impedance. Its phase line, however, might not pass through the origin but might have a certain offset $\mathscr{B}^{o'}$ if the regional vertical field is non-zero. Therefore, a shift away from the origin is an indication of the presence of a uniform regional vertical component due to a significant, large-scale vertical conductivity boundary.

If the regional vertical field is close to zero, or if difference-field transfer functions are available (where the regional vertical field is eliminated), the computed response functions represent the local response functions. Then, with reliable predictions of the local strike from surface geology or high-

frequency data, the ratio of the principal impedances may be estimated from the ratio of the predicted values at field directions parallel and perpendicular to the regional strike:

$$\frac{B_z^p(\vartheta_r)}{B_z^p(\vartheta_r + 90)} = \frac{\mathscr{A}^\ell}{\mathscr{B}^\ell} = \frac{Z_B}{Z_E} \cdot \tan\alpha. \qquad (39)$$

The frequency dependence of this ratio can be expected to be the same for all sites representing the same regional geology.

Although we are not able to determine the individual values of the principal impedances from the distorted magnetic response function, hypothetical event analysis enables us to extract their frequency variations, their phases, their ratio, and the strike direction of the regional structure in which the currents are induced.

2.2.2 Determination of the phase line

The common phase angle is determined from N data points in the complex plane by the least-squares method. In order to determine the degree of linearity of the data distribution, the correlation coefficient is estimated from the real (x) and imaginary (y) parts of all sites (Bronstein & Semendjajew 1981):

$$r = \frac{\sum (x - \bar{x})(y - \bar{y})}{\sqrt{\sum (x - \bar{x})^2 \sum (y - \bar{y})^2}}, \qquad (40)$$

where, in our case, $\bar{x}$ and $\bar{y}$ correspond to the mean values of all real and imaginary parts, respectively. If $|r|$ is found close to 1, the data are strongly correlated, whereas values close to 0 indicate a weak linear relation. Hence, this parameter can be used in HEA to find the magnetic field direction for which the data are most strongly correlated.

Since the estimation of the linear correlation coefficient depends strongly on the inclination of the phase line, we will not get an objective idea of the degree of linearity if we calculate the coefficient from the data in a fixed frame. For example, points scattering along one of the axes (for phase angles of 0° or 90°) will always deliver a correlation coefficient close to zero, even if they fall on a perfect line. However, points grouping closely along a diagonal line (phase 45°) yield a maximum coefficient near $|1|$, which is certainly a realistic estimation of their linear correlation. Thus, in order to obtain an objective correlation coefficient, it is necessary to rotate all data through a quadrant (0° to 90°) and compare only *maximum* values r_{max}. Data with low linear correlation will then still produce a low coefficient.

In practice, data distributions with $r > 0.7$ may be approximated well by linear regression lines with gradient m and intercept c for x- and y-distributions:

$$x_i = m_x y_i + c_x \qquad \text{and} \qquad y_i = m_y x_i + c_y. \qquad (41)$$

If the linear correlation is perfect ($|r| = 1$), both lines are equivalent. For relatively good correlation ($|r| > 0.8$), the lines are only slightly different. However, the smaller the correlation coefficient, the more the lines will differ. In the case of imperfect linear correlation, the line with the smaller standard deviations for the slope and intercept is chosen to represent the regional phase.

The data distribution can also be fitted by a single regression line that allows scatter in both the x- *and* the y-components.

However, we chose to compute the lines separately for *x*- and *y*-distributions in order to obtain an instant impression of the linear correlation of the data. In most cases the data distribution is approximated best by the *y*-line, because the real parts are generally larger than the imaginary parts (see e.g. Fig. 11). The *y*-lines also show the smaller standard deviations and less dramatic fluctuations with changing field directions (see e.g. Fig. 12).

2.2.3 Is the regional setting 1-D or 2-D?

From the findings in the previous sections, we can design the following tests for the dimensionality of the data.

(1) *Single site.* If we compute the ratio of the two components of the magnetic response function (or the ratio of the predicted vertical field at perpendicular directions ϑ^*), we should be able to distinguish 1-D from 2-D data. In the regional 1-D case, the ratio is real and constant over the period range of distortion, because all complex frequency-dependent information is contained in the regional impedance, which is eliminated from the ratio. We are left with the constant strike azimuth of the structure that is responsible for distortion at that site:

$$\text{1-D earth}: \quad \frac{\mathscr{A}^\ell}{\mathscr{B}^\ell} = \frac{B_z^\mathrm{p}(\vartheta^*)}{B_z^\mathrm{p}(\vartheta^*+90)} = -\tan\theta_\ell = \text{const}. \quad (42)$$

However, if the regional structure is 2-D, and the measurement is not taken in the coordinate frame of the regional strike, the ratios contain a combination of the principal impedances in both the numerator and the denominator (see eq. 24a,b). In that case the ratios are clearly complex and frequency-dependent.

(2) *Array.* If we visualize the real and imaginary parts of predicted values for the vertical field at gradually varying directions ϑ^* in the complex plane ('Argand diagram'), 1-D data will plot along a line indicating the phase of the regional impedance. The resulting 1-D phase must be independent of the direction of the horizontal magnetic field:

$$\text{1-D earth}: \quad \frac{\mathscr{I}m\, B_{z_i}^\mathrm{p}(\vartheta^*)}{\mathscr{R}e\, B_{z_i}^\mathrm{p}(\vartheta^*)} = \frac{\mathscr{I}m\, Z}{\mathscr{R}e\, Z}. \quad (43)$$

In the case of a regional 2-D structure, the distribution of the values in the complex plane is highly dependent on the azimuth ϑ^*. One should be able to determine an angle where the $B_{z_i}^\mathrm{p}(\vartheta^*)$ and $B_{z_i}^\mathrm{p}(\vartheta^*+90°)$ collapse on distinct phase lines. If the phase line is shifted away from the origin, we must assume that a regional vertical magnetic component is present in the data. The shift can be eliminated by changing the azimuth: it vanishes if the hypothetical horizontal field is directed parallel to the regional strike direction. This case corresponds to the B-polarization mode, where no vertical magnetic component is generated. On the other hand, the shift can be maximized by choosing a direction of the magnetic field that is perpendicular to the regional strike, corresponding to the E-polarization.

The existence of a shift of the phase line in the complex plane, together with the possibility of removing it, is therefore a good indiction for regional two-dimensionality of the data. Only then can a spatially uniform vertical component be present. If no phase line or strike direction can be found with this technique (i.e. the shift is not removable), one must either assume a more complex regional structure, or that the distortion model is not appropriate at all.

2.2.4 Do the data fit the distortion model?

The features used above to determine the dimensionality of the regional structure can be applied equally well to the recognition of distortion in the data, especially with respect to the variation with period. A more straightforward way to identify the period range over which current deviation causes a strong vertical magnetic field component is to investigate the variation of the magnetic response function components with period. The ratios of components at different sites ($\mathscr{A}_i/\mathscr{A}_j$) equals the ratio of their distortion parameters. They should be real, frequency-independent numbers in the period range of distortion (see Fig. 2e).

If the magnetic data have been recorded simultaneously with a reference site, magnetic response functions estimated by common reference processing can be used to detect distortion. If the spatial variations of the vertical magnetic field are caused by galvanic effects, the hypothetical event analysis of the difference field data clearly reveals two common phases. These phase angles are typically positive and in the range 0°–90°. For field directions parallel *and* perpendicular to the regional strike, the data distributions will be highly linear, and regression lines at both azimuths wil pass through the origin of the complex plane. In this case, the distortion model described in this paper is valid, and the data can be interpreted in the proposed way. However, if induction at a nearby regional boundary produces a spatially non-uniform magnetic field, the magnetic data at each site of an array are affected individually. This results in a strong scattering of the predicted vertical fields in the Argand diagrams at all directions ϑ^*, except close to the regional strike azimuth. If both effects are superimposed, and the galvanic contribution has the smaller amplitude, it will be difficult to fit regression lines for an azimuth perpendicular to the regional strike.

2.2.5 Error of the recovered regional strike azimuth

As already mentioned in Section 2.2.2, we can determine an error for the common phase from the standard deviation of the slope of the regression line. However, it is not equally straightforward to estimate a statistical error for the strike direction. The assumptions underlying the approach may not always be met exactly, neither by the data nor by the geological setting. We found that if the data are erroneous [as e.g. in Ritter & Ritter (1997) for the long periods >1000 s of the BC87 data set], their predicted vertical fields scatter in a strongly non-linear way in the Argand diagrams, and it is impossible to derive a strike direction. The strike angle is not calculated directly from the data, but determined by criteria which depend on the linear correlation of the data distribution and the position of the common phase line. The azimuth range in which the cloud of observations collapses on a straight line through the origin of the complex plane can be judged to a range of ±5°. This error can be assigned generally to the regional strike azimuth determined by hypothetical event analysis.

3 THE IAPETUS DATA SET

The application of HEA for the recovery of distorted regional information was tested against the vertical magnetic response functions of the 'Iapetus' database. The data set was compiled by Banks [see Banks *et al.* (1993) for references to sources]

and comprises 127 sites in an area that extends 200 km E–W × 300 km N–S in northern England and southern/central Scotland. The data were collected during the past 20 years; they are in the period range 20–7000 s. With an average site spacing of 10–20 km, the array covers a region associated with an ancient plate boundary, the Iapetus Suture Zone. From the surface down to the mantle, the crustal structure is of a complex nature. Distortion due to current deviations is therefore a very likely phenomenon at all levels in the crust, and problems such as static shift have been discussed for electromagnetic data in the whole region (Harinarayana *et al.* 1993; Sule *et al.* 1993; Banks *et al.* 1996; Junge 1995). In addition, current concentrations in the shallow and deep seas and seafloors around the British Isles may contribute to distortion effects.

The Iapetus Suture marks the join of two formerly separate continental plates, welded by the closure of the Palaeozoic 'Protoatlantic', the Iapetus Ocean. During the late phase of the closure, numerous granitic intrusions were emplaced on both sites of the suture, creating a *block-and-basin* structure (Bott 1967). As a consequence, major fault systems developed at the edges of the Devonian batholiths and various sedimentary basins were filled during the Upper Devonian, the Carboniferous and later (see the overview map in Fig. 4). The most prominent is the E–W-striking Northumberland Trough in northern England, which is thought to conceal the assumed Iapetus Suture Zone. Reaching a width of up to 30 km, the trough stretches on land over 100 km from the North Sea in the east to the Solway Firth and Irish Sea in the west. Its marine continuations to the east and west are thicker and more extensive than the sediments on land. To the north and south, the Northumberland Trough is bounded by the Southern Uplands and the Alston Block, respectively. On its southern edge the sediments reach a thickness of up to 4 km.

The crust of the whole region has been investigated intensively over the past few decades by geophysical methods.
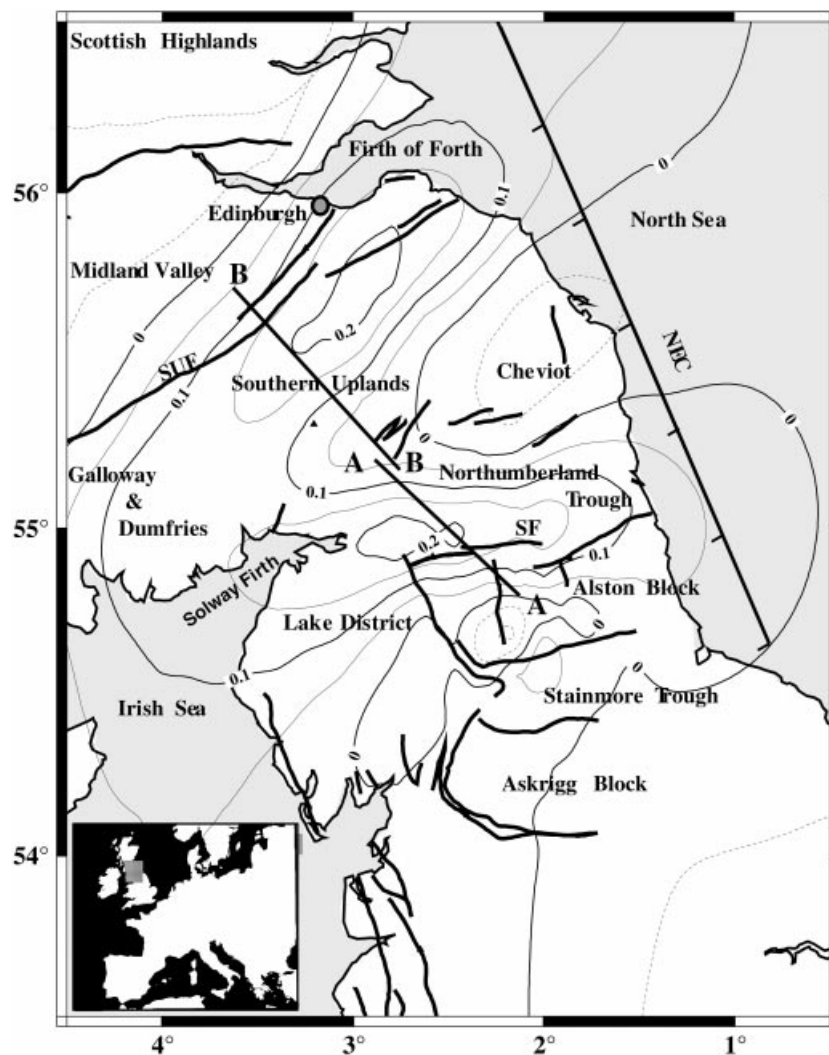

Figure 4. Summary map of the Iapetus Suture Zone (based on Banks *et al.* 1996). The major faults are marked by heavy lines: SUF, Southern Upland Fault; KF, Kingledores Fault; SF, Stublick Fault. The contours show the horizontal component of the magnetic variation anomaly at a period of 250 s and delineate the crustal conductors. BB′, AA′ is the MT profile of Banks *et al.* (1996). NEC is the seismic reflection profile. The region is characterized by a typical block- and-basin structure. The granite batholiths are the Weardale granite underlying the Alston Block, the Wensleydale granite underneath the Askrigg Block, the Cheviot granite beneath the volcanic Cheviot Hills, the Shap, Skiddaw and Eskdale granites beneath the Lake District, and the Doon, Criffel and Cairnsmore of Fleet granites in Dumfries and Galloway (Leeder 1982; Livelybrooks *et al.* 1993).

A detailed and up-to-date overview can be found e.g. in Livelybrooks *et al.* (1993) or Banks *et al.* (1996). Results of various GDS surveys indicate two lateral conductive features. The northern anomaly trends obliquely (NNE) to the Southern Upland Fault; the southern one is correlated with the E–W extension of the Northumberland Trough. The junction of the two anomalies is near Dumfries (SW Scotland).

The vertical magnetic field component is strong north and south of the Northumberland Trough and induction arrows over the whole period range indicate clearly the E–W-striking conductor (Fig. 5 for $T = 750$ s). Beamish & Banks (1983), Banks (1986) and Banks *et al.* (1993, 1996) pointed out that the anomaly associated with the Northumberland Trough is produced in part by current concentrations in the surface sediments but mainly in the mid-crustal conductor. From hypothetical event maps of a magnetometer array across the

Alston Block (53 sites), Banks & Beamish (1984) concluded that, at periods around 1000 s, current channelling rather than induction is the ruling physical process in these extended structures. The data array studied here is an extension of that examined by Banks & Beamish.

3.1 Vertical magnetic response functions

For all sites (locations marked in Fig. 5) *single-site* vertical response functions are available. Additionally, difference field response functions ($=local$ response functions $\mathcal{A}^\ell$, $\mathcal{B}^\ell$) were computed for 35 sites on dense profiles covering an area of approximately 40×40 km across the Alston Block (Beamish & Banks 1983). They were obtained by relating the differences of total and reference vertical fields at each site ($B_{z_i}^\ell = B_{z_i} - B_z^r$) to the horizontal field at a common reference
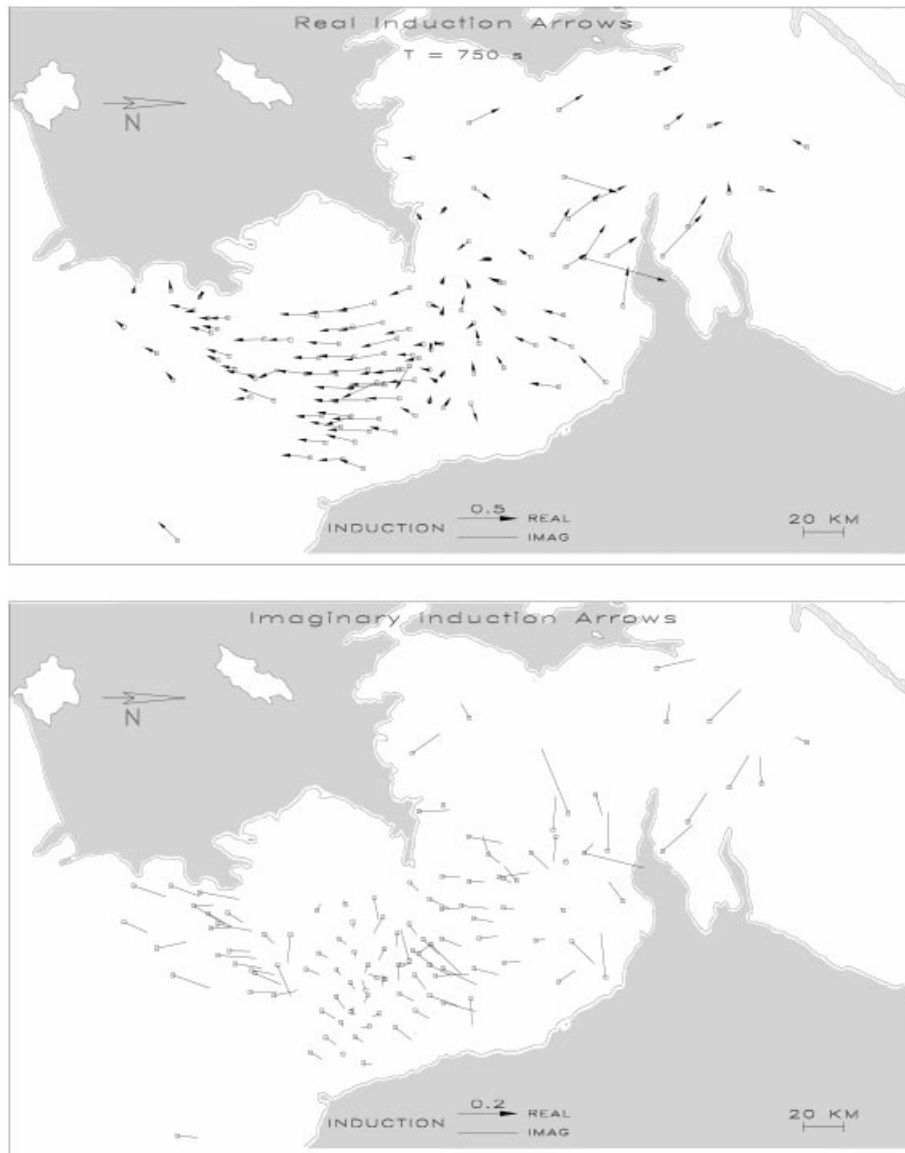

Figure 5. The Iapetus data set: induction arrows at $T = 750$ s. The uniformly strong real arrows (upper figure) across the Alston Block indicate an E–W-striking conductor in the area of the Northumberland Trough. A further NE–SW current flow may be inferred oblique to the Southern Upland Fault from a distinct change in directions across this region. The less uniform directions of the imaginary arrows (lower figure) do not agree with a 2-D conductivity distribution, and indicate a more complex crustal structure.
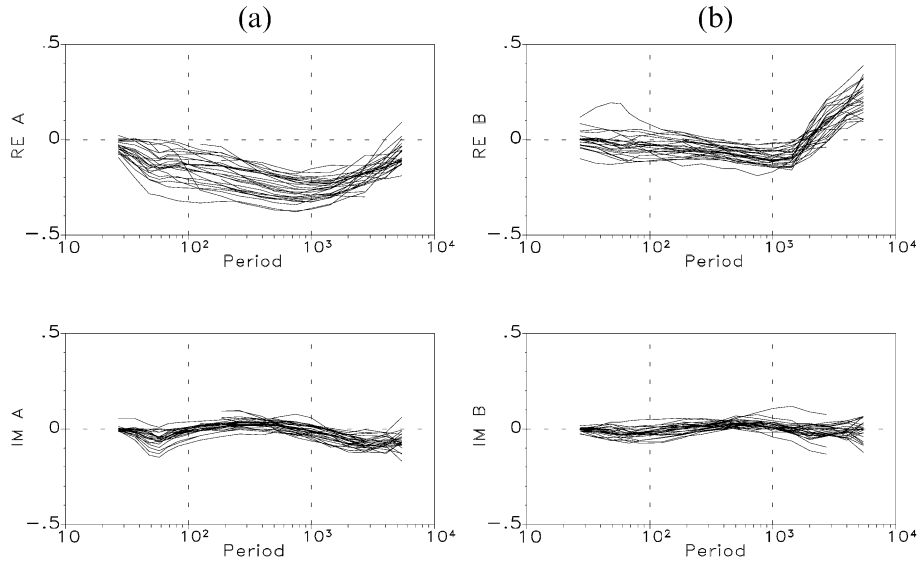
Figure 6. Real and imaginary parts of the magnetic response functions (rotation: 0°N) of sites across the Alston Block and Stainmore Trough.

site ($B^{\ell}_{z_i} = \mathscr{A}^{\ell} B^{r}_{x} + \mathscr{B}^{\ell} B^{r}_{y}$). The reference station was Durham (DM) at the eastern edge of the array. Under the assumption that the anomalous field at the reference site is small, this procedure should eliminate any contribution of the regional vertical magnetic field and reveal the *local* anomalous vertical field at each site $B^{l}_{z_i} \approx B^{a}_{z_i}$. In the following, if not stated otherwise, 'magnetic response functions' are always single-site response functions.

We used the Iapetus single-site response functions as an example data set to demonstrate the applicability of our method to real data. Like any data set of considerable size, these data certainly contain contributions from non-uniform horizontal fields and noise; that is, they may not meet all conditions required by the theoretical model. In our case, however, we can check and test the single-site results against

the more suitable interstation response functions. In Fig. 5, the induction arrows of all sites at $T = 750$ s are presented. A comparison with the 35 *relative* induction arrows across the Alston Block at the same period showed only small differences (Ritter 1996). It may be concluded that the requirement of quasi-uniform fields is met at least in this area. The variation of the horizontal fields among these sites is less than 20 per cent (Banks & Beamish 1984).

3.1.1 Period dependence of the magnetic response functions

Figs 6 and 7 show the variations of the magnetic response functions ($\mathscr{A}_i$, $\mathscr{B}_i$) and, for comparison, the *local* response functions ($\mathscr{A}^{\ell}_i$, $\mathscr{B}^{\ell}_i$) of sites situated across the Alston Block. The curves in the top figures are generally representative of
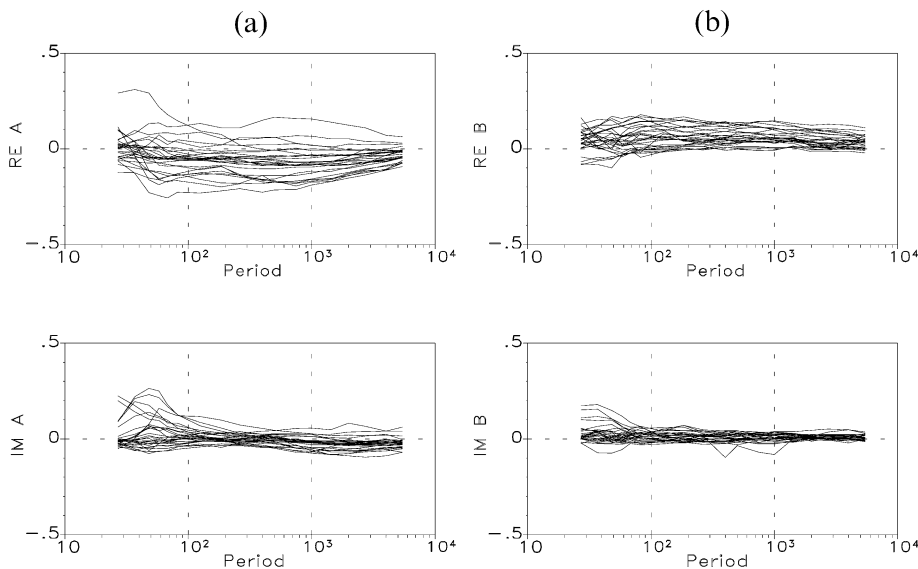

Figure 7. Real and imaginary parts of the *local* magnetic response functions calculated from difference fields (rotation: 0°N) of the Alston Block data set. Apart from the shortest periods, the curves of different sites are parallel. Their variations are smaller than those of the single-site response functions because the contribution of the regional vertical component is eliminated.

sites situated south of the Southern Upland Fault. Although the amplitudes may vary between sites and areas, $\mathscr{A}_i$ and $\mathscr{B}_i$ run in smooth, descending curves in the intermediate-period range 400–2000 s. Differences between the components can be observed in the adjacent period ranges, especially at the longest periods, where the curves of the real parts ascend. From the change of the amplitude ratio between the two components $\mathscr{A}$ and $\mathscr{B}$, a change of the inherent coordinate system (i.e. strike direction) with increasing period may be inferred. The imaginary parts also tend to rise slightly towards the longest periods. In this period range currents are presumably induced in the upper mantle, or possibly in the deep ocean and underlying oceanic crust and mantle to the west and southwest of the British Isles.

At short periods around 60 s, a small negative peak can be detected in the real and imaginary parts of many sites, indicating an inductive response in this range. Depending on the assumptions made for the resistivity of the crust, a structure causing this effect in the response functions would be situated in the middle crust (skin depth is *ca.* 12 km for 10 Ω m). If the smooth curves in the intermediate-period range are produced by channelling of regional currents through the mid-crustal conductor, the corresponding induction arrows may reflect only the strike of this *local* body.

The maxima at short periods around 60 s are also present in the *local* response functions ($\mathscr{A}_i^\ell$, $\mathscr{B}_i^\ell$) in the lower graphs. At long periods ($T > 1000$ s), the $\mathscr{R}e\,\mathscr{A}_i$ plots converge towards zero. However, the negative maximum of $\mathscr{R}e\,\mathscr{A}_i$ stretching over the intermediate-period range and the steep rise of the $\mathscr{R}e\,\mathscr{B}_i$ have disappeared altogether. According to the theory presented in the previous section, the remaining smooth curves in the period range 200–1000 s may contain the two principal impedances, Z_B and Z_E. They may be scaled up or down by real factors of position. The difference between *local* and single-site magnetic response functions requires the presence of a regional vertical component B_z^o. This can only be produced by a significant, laterally bounded regional structure.

As stated in Section 2.2.4, we would expect the ratios of the magnetic response functions of different sites to be frequency-independent and real in the period range of distortion. In Fig. 8, we show the ratios of the components $\mathscr{R}e\,\mathscr{A}_i/\mathscr{R}e\,\mathscr{A}_j$ and $\mathscr{I}m\,\mathscr{A}_i/\mathscr{I}m\,\mathscr{A}_j$ and those of $\mathscr{R}e\,\mathscr{B}_i/\mathscr{R}e\,\mathscr{B}_j$ and $\mathscr{I}m\,\mathscr{B}_i/\mathscr{I}m\,\mathscr{B}_j$ of the *local* response functions of the Alston Block array. They were all computed relative to one central station (index j). Between 400 and 1500 s, the ratios of the real parts of both components are constant, almost parallel and of similar amplitude. Similar behaviour can also be found, but is less clear, in the imaginary parts of $\mathscr{A}$. In that period range the imaginary parts are generally smaller than the real parts. These observations clearly indicate that galvanic effects are occurring in the period range 400–1500 s.

3.2 Hypothetical event analysis

The theoretical analysis of the vertical magnetic response function showed that in the case of galvanic distortion, the phase content of the predicted vertical magnetic field B_z^p obtained by applying hypothetical event analysis will be that of the regional impedances. Assuming quasi-uniform fields over the area under investigation, this information and the regional strike should be retrievable when the predicted values of all GDS stations are displayed in the complex plane (Argand diagram).

Fig. 9 shows the predicted vertical fields of all 120 sites at four periods and at two perpendicular directions ϑ^*. In the left column, the hypothetical horizontal magnetic field is directed northwards (0°), whereas the values of the right column were calculated assuming an eastward-directed field (90°). At these two azimuths the predicted values correspond to the $\mathscr{A}$ and $\mathscr{B}$ components of the magnetic response function.

We would expect the data points to range along phase lines. However, this is not always obvious. Instead, the data scatter strongly, forming clouds of points that in places do have certain orientations. Generally, the clouds seem more
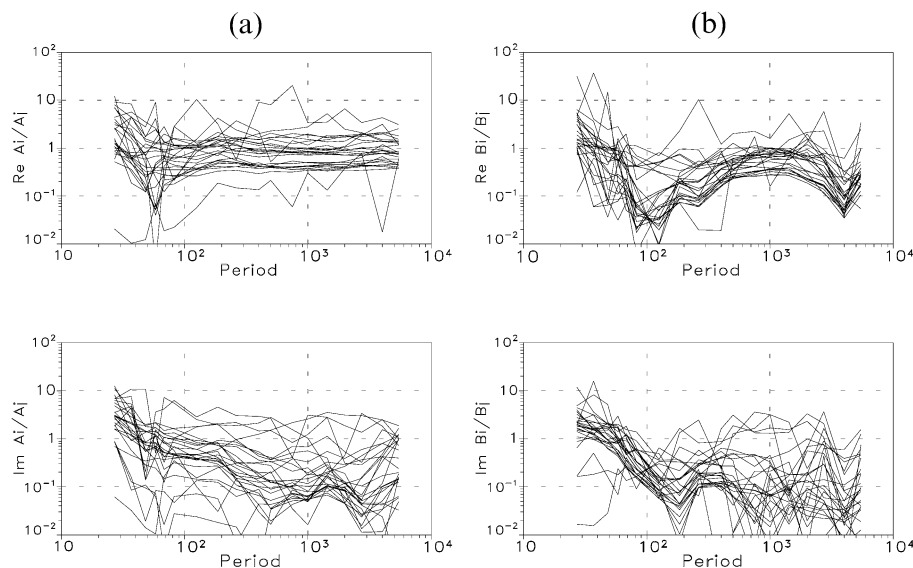

Figure 8. Ratios of the *local* magnetic response functions of all sites of the Alston Block data set with respect to one site in the centre of the array. At periods of 400–1500 s, the ratios of the real parts of both components are relatively constant, suggesting that distortion processes are affecting this period range.
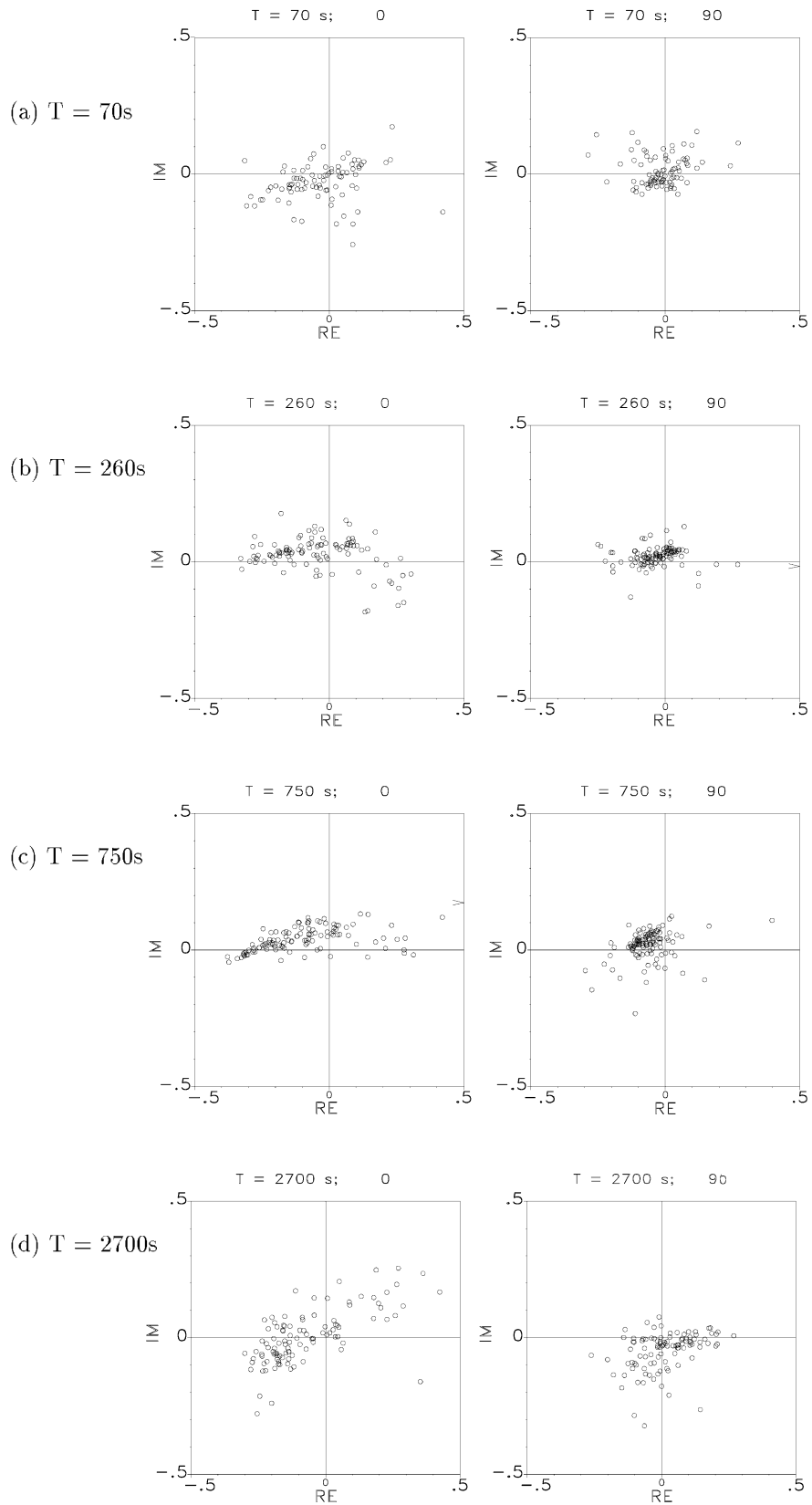
Figure 9. The Iapetus data set: hypothetical event analysis of all sites at four periods. Argand diagrams of predicted values $B_{z_i}^p$ are shown at periods $T = 70, 260, 750, 2700$ s, estimated for the northward direction ($\vartheta^* = 0°$, left column) and the eastward direction ($\vartheta^* = 90°$, right column) of the hypothetical horizontal magnetic field. If the field is directed northwards the points plot roughly along lines indicating the regional impedance phase (except for the longest period).
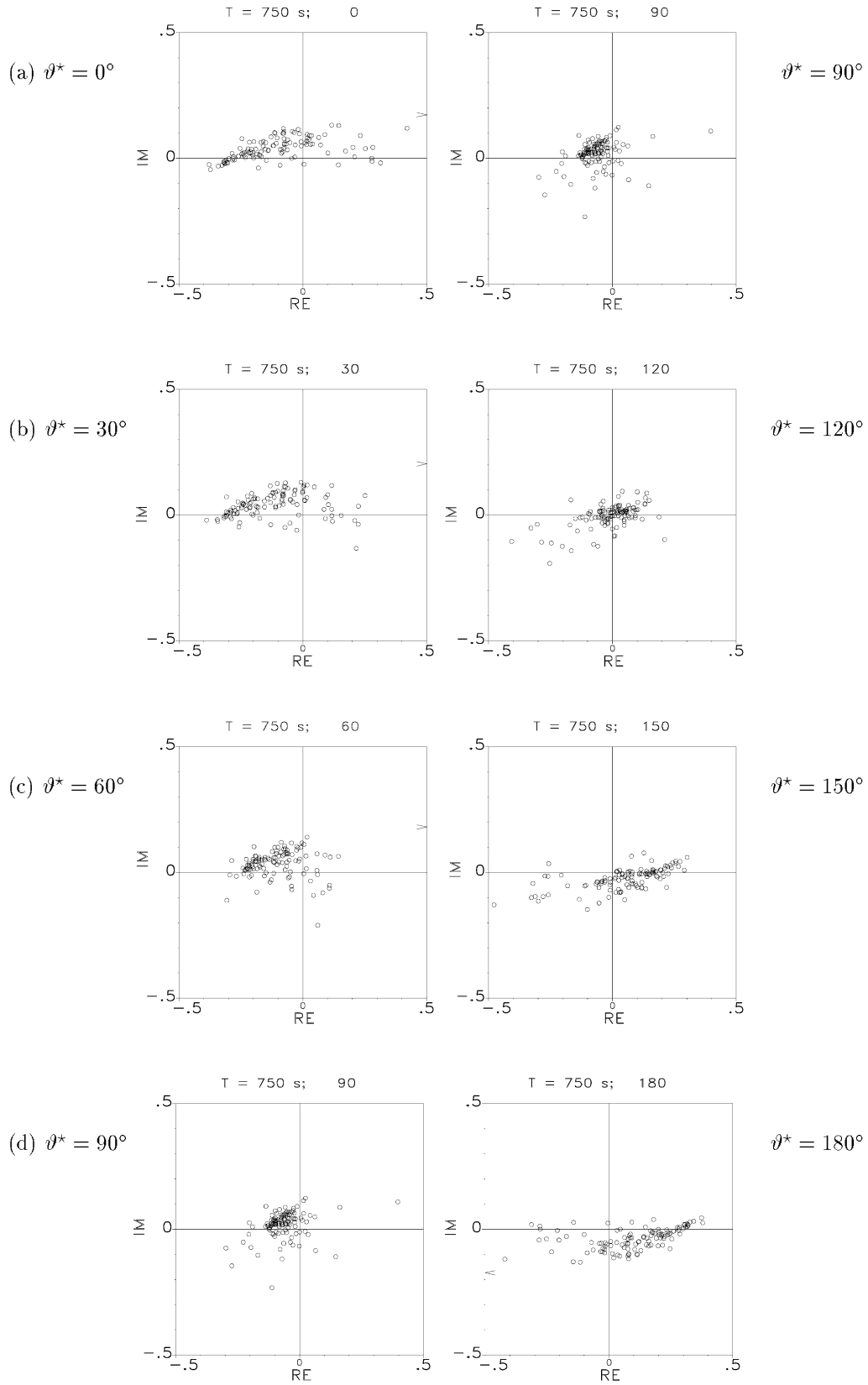
Figure 10. Hypothetical event analysis of all sites at $T = 750$ s. The Argand diagrams of the predicted values $B^p_{z_i}$ are estimated for directions $\vartheta^* = 0°$, $30°$, $60°$, $90°$ (left column) and perpendicular (right column) to these. The cloud of points passes through the origin at $\vartheta^* = 120°$.

elongated in the left column of Fig. 9, while in the right column the predicted values are rather focused on patches close to the origin. At periods of 260 s (b) and 750 s (c) the phase lines can be characterized by a positive slope of *ca.* 15°–20° for the northward-directed field. The fact that they do not pass through the origin hints at the presence of a regional vertical field. Linear trends, if less clear, can also be recognized for the eastward direction at 260 and 750 s. The gradient at 750 s is steeper, but less focused. At all four periods, the outliers are limited to a fairly restricted area in the complex plane. Most of them belong to sites in the same geographic region, north of the Southern Uplands.

The next step of the data analysis is to examine the period range where distortion is suspected. We chose 750 s as a representative period of the distortion range found earlier. Fig. 10 shows the results of hypothetical event analysis with respect to varying directions of the horizontal magnetic field. With gradually changing azimuths, the data points move across the complex plane, always forming one coherent cloud of points. The direction at which the imagined line actually passes through the origin seems to be $\vartheta^* = 120°$. At this azimuth, most points plot densely on a short line with a gradient of *ca.* 10°. At 90°, just before passing the origin, the cloud contracts to a small, almost round patch. The linear distribution seems to be best in the northward direction.

The variable form of the cloud and the fact that the offset from the origin can be eliminated by choosing an appropriate azimuth ϑ^* strongly suggest a regional 2-D structure. As a consequence, the azimuthal range where the line passes through the origin and the range perpendicular to that may be interpreted in terms of a regional strike direction (Section 2.2, 2-D) and thus demands more detailed investigation. The gradients of the lines at these azimuths provide the phase angles of the two principal impedances. In the following the data were fitted by regression lines as explained in Section 2.2.2.

3.2.1 Reduced data set

The linearity of the data distributions was improved by investigating subsets of data according to their geographic locations. The northernmost sites were omitted and hypothetical event analysis was applied to the reduced data set. The predicted vertical magnetic fields of the remaining 95 sites (all located south of the Southern Upland Fault) are shown in Fig. 11 for field directions of 33° and 123°. As expected, the remaining 95 data points are less widely scattered. Each graph contains the two regression lines computed for the *x*- and *y*-distribution of the data (see Section 2.2.2). The solid regression line has a minimum offset from the origin at the azimuth 123°. Its gradient is $12.6° \pm 2.5°$ (phase of Z_B). At an azimuth of 33°, the solid *y*-line has a slope of $14.6° \pm 1.6°$ (phase of Z_E).

The two regression lines differ in accordance with the degree of linearity of the data. The only objective criterion to choose between the *x*- and *y*-lines is the standard deviation. The regression line properties for both lines are shown in Fig. 12 for varying azimuths in the range 0°–180° (estimated at steps of 5°).

Both correlation coefficients, r and r_{max}, (see Section 2.2.2) run in almost parallel curves and indicate high linear correlation at most directions, except for a minimum in the range around 100° (Fig. 12a). At an azimuth of 123°, at which the cloud of points passes the origin, the more significant r_{max} has recovered to values >0.7. In general, the standard deviation of the *y*-line (solid) is smaller than that of the *x*-line (dashed). Characteristically, its largest deviations occur at around 100°, the minimum of the linear correlation coefficient r. The offset of the *y*-regression line (Fig. 12c) is also distinctly smaller than that of the *x*-line. c_y is at a maximum when the magnetic field is directed at 35° (i.e. perpendicular to the minimum offset). The slope of the *y*-line varies little, between 12° and 15°, over the whole azimuth range (Fig. 12d), whereas the gradient curve of the *x*-line shows fairly strong variations.

The less dramatic fluctuations of the characteristics of the *y*-line and its lower errors at all field directions make this regression line the better representative of the trend observed in the data set. We found that the strike direction of the inferred regional structure has to be amended slightly towards 125°. A further subset will provide more accurate values for the regional strike and impedance phase angles: the Alston Block data set.

3.2.2 Alston Block data

The hypothetical event analysis of the Alston Block data set provides the most reliable value for the regional strike azimuth as its linearity is high ($r_{max} > 0.8$ at most field directions)
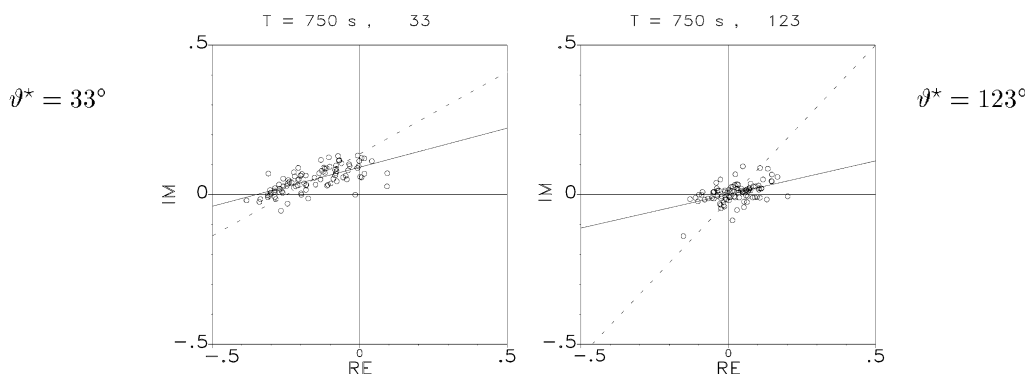

$\vartheta^\star = 33°$ T = 750 s, 33   T = 750 s, 123 $\vartheta^\star = 123°$

Figure 11. Hypothetical event analysis of the reduced data set (95 sites) at $T = 750$ s. All sites are located south of the Southern Upland Fault. The predicted values $B^p_{z_i}$ were computed at the azimuth of minimum offset, 123°, and perpendicular to it, at 33°. Regression lines: dashed = *x*-line; solid = *y*-line. The linearity of the data distribution is improved compared to that of the original data set (113 sites).
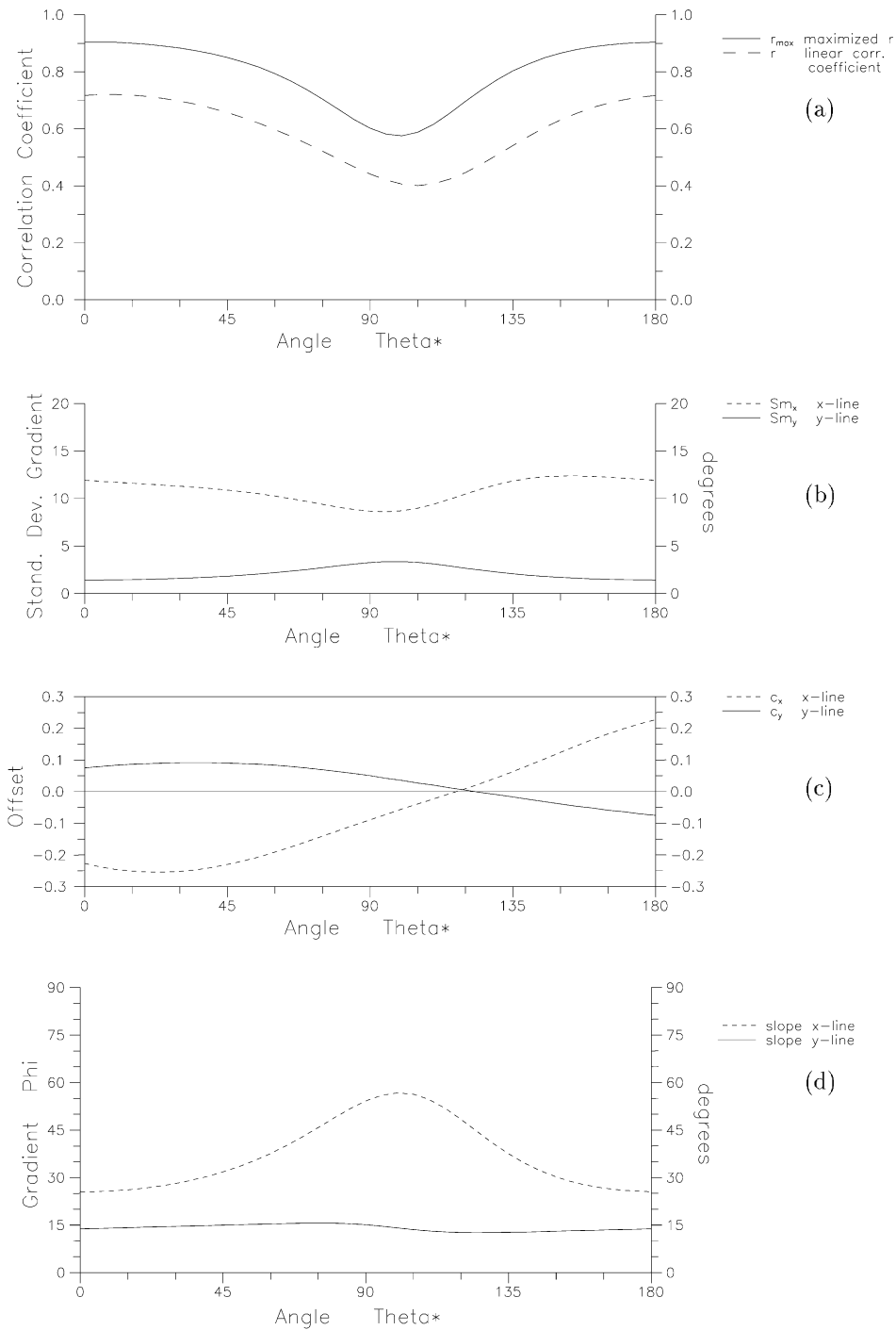
Figure 12. Regression line parameters computed for the data (95 sites) at $T = 750$ s; field directions are 0°–180°. (a) Linear correlation coefficients $|r|$ (dashed line) and $|r_{max}|$ (solid line). (b) Standard deviations of the gradients of the x-line (dashed) and y-line (solid). (c) Intercepts (offsets) of the x-line (dashed) and y-line (solid). (d) Phase angles inferred from the gradients of the x-line (dashed) and y-line (solid).

compared to the larger data sets. Fig. 13 shows the predicted vertical fields calculated from the single-site response functions at the azimuth of minimum offset (y-line) at 130° and in the perpendicular direction, at 40°. The phase line indicated by these data points is clearer than in the larger data sets, especially in the azimuth range where the line passes through the origin. Owing to the improved linearity of the data distribution, the x- and y-lines are in better agreement. The regional strike direction indicated by the azimuth of zero-offset is 130°.

The phase angles, on the other hand, are best determined from the *local* response functions because any contributions from a regional magnetic field is eliminated. As a consequence, the offset of the regression lines is reduced considerably. This can be observed clearly in Fig. 14. The general linear correlation of these data is very good, with values of r_{max} at 0.96 for most directions of the magnetic field. The slopes of the phase lines are $19.9° \pm 2.3°$ at an azimuth of 40°, and $10.5° \pm 1.5°$ when the field is directed towards 130°. These
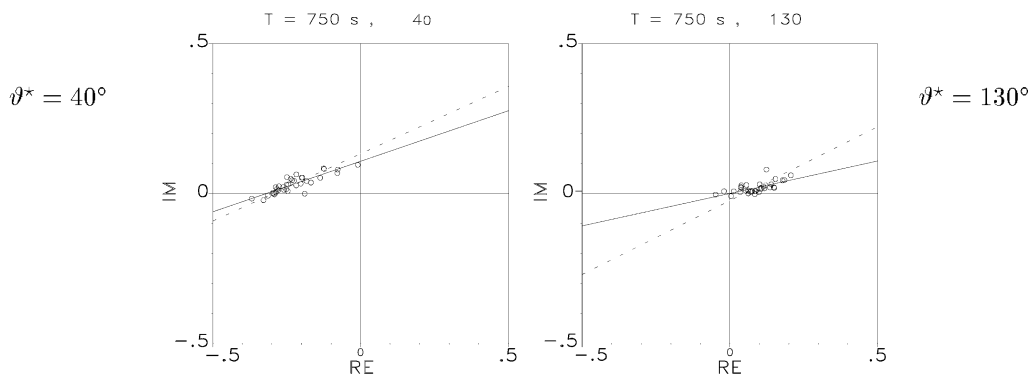
Figure 13. Hypothetical event analysis of the Alston Block data set (35 sites) at $T = 750$ s. The sites are located directly south of the Northumberland Trough. The predicted values $B_{z_i}^p$ are shown at the azimuth of minimum offset, 130°, and perpendicular to it, at $\vartheta^* = 40°$. The azimuth of minimum offset yields the regional strike direction. The fitting of the regression lines has improved considerably compared to the larger data sets (113 sites and 95 sites). Regression lines: dashed = x-line; solid = y-line.

gradients provide the values for the regional impedance phase angles of the E- and B-polarization modes, respectively.

Because the phase difference between the two impedances is only very small, it cannot be resolved as clearly within the larger data sets where the points scatter more. In addition, the outliers are clearly not distributed randomly. As a consequence, data points that are either extremely noisy or contain different electromagnetic information due to their geographic location will bias the least-squares estimation of the regression lines, i.e. the phase angles. However, if we remove only the four worst outliers of the larger data set of Fig. 11, the remaining 91 sites already show a clear phase difference of 6°.

3.2.3 *Investigation of the whole period range*

In the previous sections we concentrated mainly on the analysis of the data sets at one period (750 s). It is now interesting to find out whether the observations can be generalized to the whole period range for which distortion is assumed. The following multifrequency investigations are focused on the Alston Block data. The contour maps of Fig. 15 show the variations of the maximized linear correlation coefficient r_{max} and of the offset (y-lines) throughout the period range 30–5500 s. The directions of the hypothetical horizontal

magnetic field vary in the range 0°–180°. Due to the very low linear correlation at 5500 s ($r_{max} \approx 0.1$), results in the upper period range should not be paid too much attention; the same is true for the shortest period of 30 s.

Throughout the period range 70–1500 s, the linear correlation coefficient r_{max} (Fig. 15a) follows the pattern already found for the period 750 s (see Fig. 12a). The minimum occurs generally at field directions in the narrow range of 90°–105°, whereas the correlation is very good (> 0.95) for azimuths $< 45°$ and $> 135°$. At periods exceeding 1000 s, the minimum expands towards smaller azimuths (upper left corner). However, the most important feature is the uniform behaviour of the linear correlation coefficient between 250 and 1000 s, not surprisingly in the same range where galvanic distortion is suspected.

The offset of the regression line (Fig. 15b) shows an equally clear pattern, but over a more restricted period range. The zero contour, where the regression line passes through the origin, occurs consistently at field directions between 125° and 135° in the period range 400–1500 s. The azimuth range of maximum offset (≈ 0.1) is at around 45°, i.e. approximately perpendicular to the position of the offset minimum. The contribution of the regional vertical magnetic component, which causes this offset, seems to be stable over this period range. This implies that both the distortion process and the contributions from regional
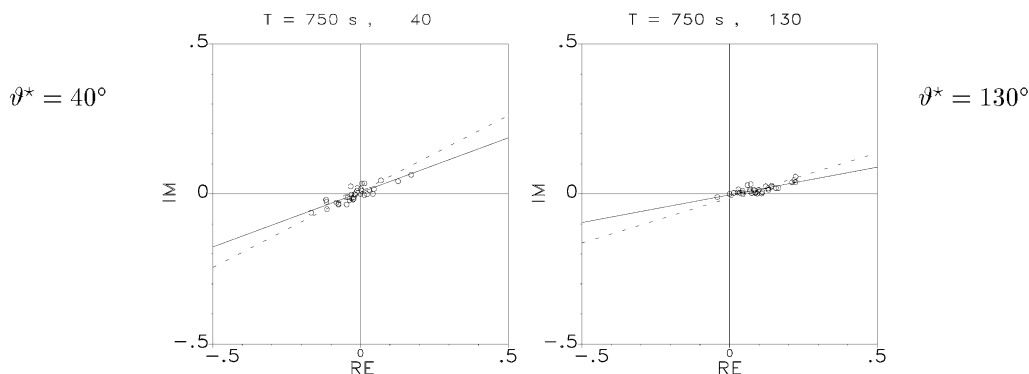

Figure 14. Hypothetical event analysis of the *local* response functions from difference fields of the Alston Block data set (35 sites) at $T = 750$ s. The Argand diagrams show the predicted values $B_{z_i}^p$ at $\vartheta^* = 40°$ and at $\vartheta^* = 130°$ (see previous figure). Since the contribution of the regional vertical component is minimized for the difference field data, all y-lines pass through the origin, and the impedance phases can be determined best using this data set.
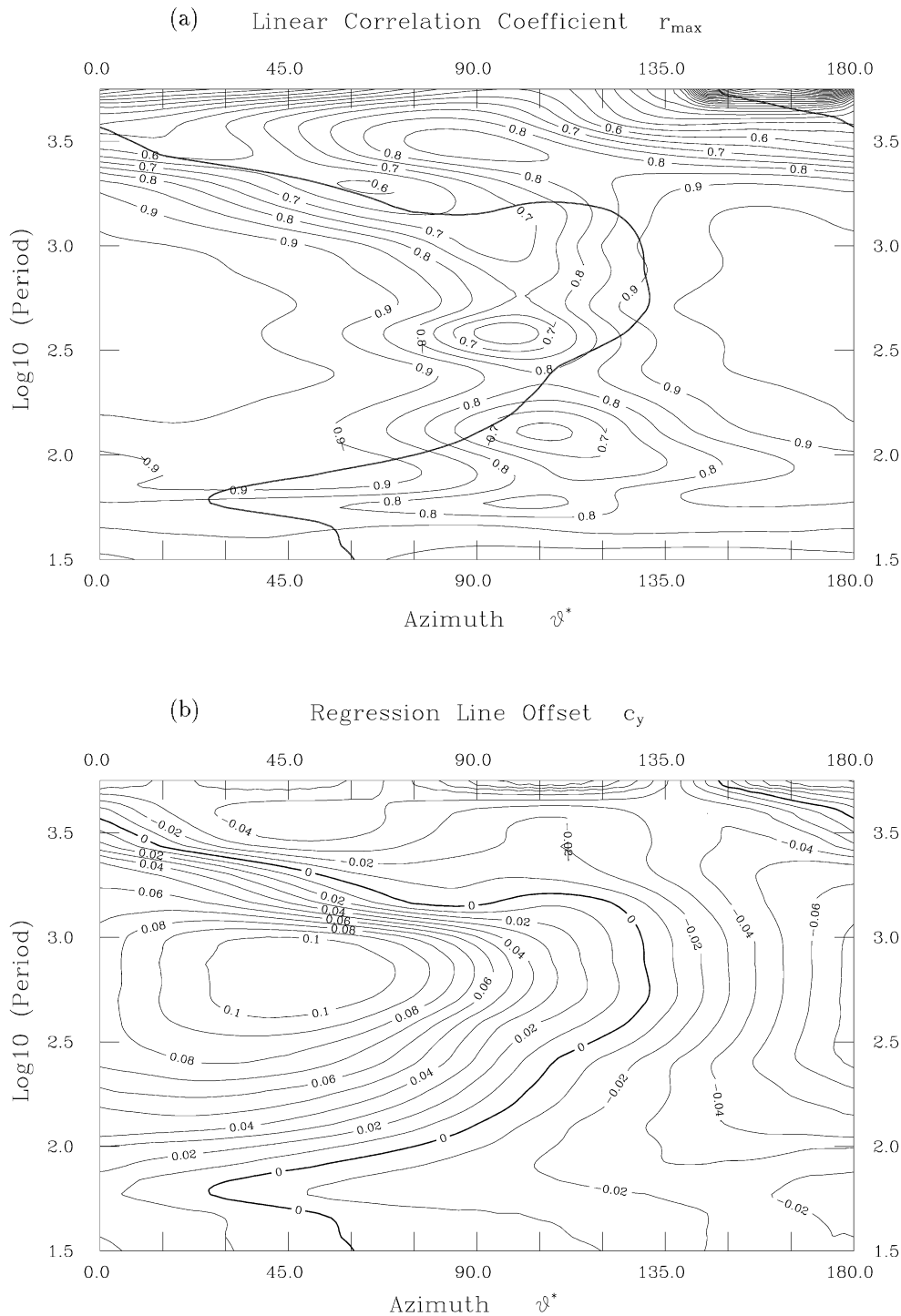
(a)   Linear Correlation Coefficient r_{max}

(b)   Regression Line Offset c_y

Figure 15. Hypothetical event analysis of the Alston Block data set at all periods for field directions 0°–180°. Map (a) shows the contour plots of the maximized linear correlation coefficient $|r_{max}|$. The thick line marks the positions of the zero-offset line taken from the associated intercept map (b). The correlation minimum occurs if the magnetic field is directed at 90°–100° in the period range <1000 s. At periods of 40s–1500 s, the zero-offset line runs on the right flank of the correlation minimum in a fairly narrow band between azimuths of 125° and 133°. The zone of maximum offset is located at a perpendicular azimuth. Note that in this and the following maps the period increases from the bottom to the top of each diagram (contrary to the usual convention).

induction contained in the distorted response functions are steady over this period range and over the area covered by these data sets.

At periods $T < 80$ s the minimum/maximum pattern of the offset has vanished completely. Interestingly, at long periods ($T > 2000$ s) the positions of minimum and maximum values are reversed: the zero line now runs towards the upper left corner of Fig. 15(a), and a negative maximum occurs at 135° (upper right corner). This change indicates that the processes or structures producing the response functions at these high periods are different from those presumed to operate in the intermediate-period range of distortion.

The contour maps of the single-site data sets indicate clearly and consistently that the regional structure is of a 2-D nature and strikes N130°E. For the best determination of the regional impedance phases we examined the predicted vertical fields of the *local* response functions. Fig. 16 shows the contour map of the slope angles (i.e. phase angles) of the *y*-regression lines. The zero-offset line of Fig. 15(b) is added for reference. In the period range 200–1500 s, we can recognize a pattern of larger angles on the left side and smaller values on the right side along the zero-offset line. Values on the left side range from 4° up to 24° for Z_E with increasing periods. The phase of Z_B is more constant in this range; it takes values of 8°–16°. The phase angles of Z_E and Z_B are taken at field directions corresponding to maximum/minimum offset of the single-site data, i.e. at azimuths of 40° and 130°.

4 CONCLUSIONS

The phase content of a GDS array holds the key to recovering the regional strike direction from distorted magnetic response functions. The sign of the phase angles of $(\mathscr{A}, \mathscr{B})$ indicates whether the anomalous magnetic field is produced by induction or by distortion processes. In the latter case the magnetic phases equal the regional MT impedance phases. Using hypothetical event analysis, the phases of Z_E and Z_B can be determined with respect to the direction of the magnetic source field. This method can thus be used to recover the hidden regional strike azimuth. The regional strike is reliably retrievable even in situations where the assumptions made for the basic physical distortion model are not met exactly: this is true for inductive processes that cause uniform but negative phases across the data array, and also for non-uniform regional fields. Furthermore, the technique can also detect the regional strike

in those cases where the two principal impedance phases are very similar, causing a failure of the phase criterion of the MT decomposition methods (e.g. Bahr 1988).

The method has been tested against the GDS data of the Iapetus array. At sites in the northern part of the array, the large amplitudes of the magnetic response functions at long periods indicate inductive processes probably related to deep-seated structures associated with the NE-striking Southern Upland Fault. The induction arrows of sites located south of the Southern Upland Fault indicate current concentrations along the E–W strike of the Northumberland Trough. At periods of around 400–1500 s, the predicted vertical fields of the hypothetical event analysis reveal a common strike direction of *ca.* N125°E ($\pm$5°) in this area. The uniform behaviour of the magnetic response functions and the presence of a positive common phase in the array indicate that, in this period range, the data are affected by distortion processes. The regional strike azimuth of 125°, however, cannot be correlated with one single crustal feature, but is a result of induction in the complex deep crustal structure of the Iapetus Suture Zone and the deep ocean to the west and southwest of the British Isles. The impedance phases determined using difference field (i.e. *local*) response functions are 12°–24° for Z_E and 8°–16° for Z_B.

The regional phases are in general agreement with, but slightly lower than, recent MT results in this area. Banks *et al.* (1993, 1996) and Junge (1995) determined the impedance phases in the period range 400–2000 s at *ca.* 25° (for directions 50°–90°) and *ca.* 40° (for directions -40°–0°). These low phase values are assigned to the boundary separating the mid- or lower-crustal conductor from the more resistive basement. Regional strike directions in this period range were determined from MT data at 50° (Banks *et al.* 1996) or 65° (Junge 1995)
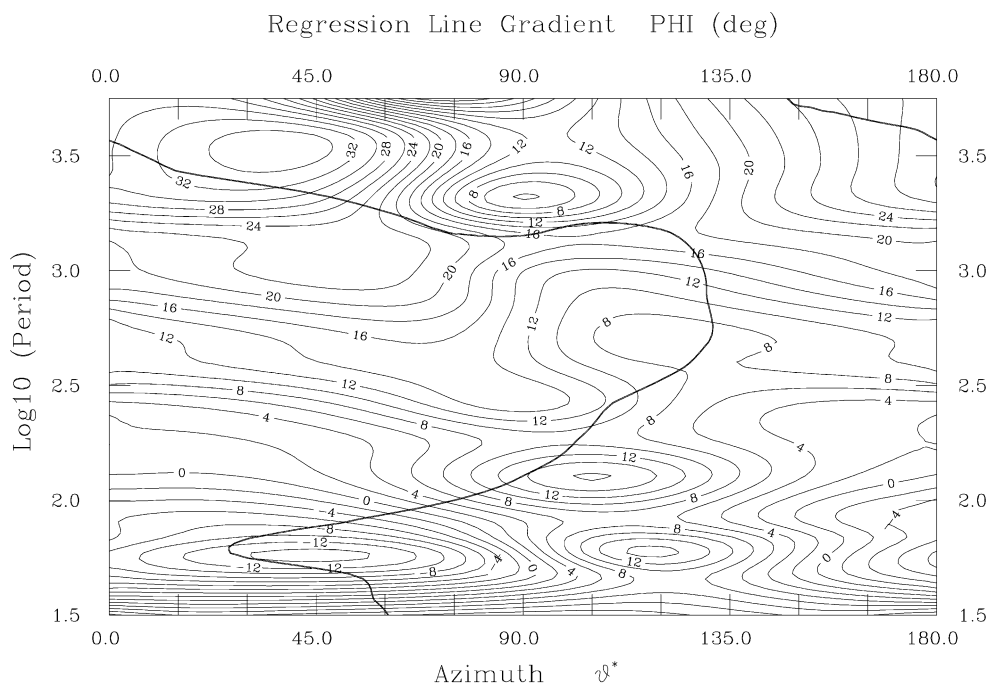

Regression Line Gradient PHI (deg)

Figure 16. Hypothetical event analysis of the local response functions of the Alston Block data set, at all periods, for field directions 0°–180°. The contour map shows the phase angles of the regional impedance inferred from gradients of the *y*-regression lines. The thick line marks the position of the zero-offset line taken from the single-site intercept map (Fig. 15b). It runs on the right flank of the correlation minimum at periods of 400–1000 s. In that range, phases are distinctly smaller along the zero-line than at perpendicular azimuths.

for the northern part of the array (Southern Uplands and northwards), and at 90° (Banks *et al.* 1996) for the southern area (Northumberland Trough and southwards).

We should like to emphasize that, if possible, *local* response functions should be used to improve the results of our technique. With new instrumentation for time-synchronous measurements now available (e.g. S.P.A.M. MkIII, Ritter & Dawes 1992), its application can also be extended to the short-period range. Ritter *et al.* (1998) showed that the vertical magnetic fields in the AMT frequency range may be used effectively for the dense mapping of shallower upper-crustal structures.

ACKNOWLEDGMENTS

REFERENCES

Bahr, K., 1985. Magnetotellurische Messungen des Elektrischen Widerstandes der Erdkruste und des oberen Mantels in Gebieten mit Lokalen und Regionalen Leitfähigkeitsanomalien, *PhD thesis,* G. August Universität Göttingen.

Bahr, K., 1988. Interpretation of the magnetotelluric impedance tensor: regional induction and local telluric distortion, *J. Geophys.,* **62,** 119–127.

Bailey, R.C., Edwards, R.N., Garland, G.D., Kurz, R. & Pitcher, D., 1974. Electrical conductivity studies over a tectonically active area in Eastern Canada, *J. Geomag. Geoelectr.,* **26,** 125–146.

Banks, R.J., 1986. The interpretation of the Northumberland Trough Geomagnetic Variation Anomaly using two-dimensional current models, *Geophys. J. R. astr. Soc.,* **87,** 595–616.

Banks, R.J. & Beamish, D., 1984. Local and regional induction in the British Isles, *Geophys. J. R. astr. Soc.,* **79,** 539–553.

Banks, R.J., Irving, A.A.K. & Livelybrooks, D.W., 1993. The simulation of magnetic variation anomalies using single station data, *Phys. Earth planet. Inter.,* **81,** 85–98.

Banks, R.J., Livelybrooks, D.W., Jones, P.C. & Longstaff, R., 1996. Causes for high crustal conductivity beneath the Iapetus Suture Zone in Great Britain, *Geophys. J. Int.,* **124,** 433–455.

Beamish, D. & Banks, R.J., 1983. Geomagnetic variation anomalies in Northern England: processing and presentation of data from a non-simultaneous array, *Geophys. J. R. astr. Soc.,* **75,** 513–539.

Bott, M.H.P., 1967. Geophysical investigations of the northern Pennine basement rocks, *Proc. Yorks. Geol. Soc.,* **36,** 139–168.

Bronstein, I.N. & Semendjajew, K.A., 1981. *Taschenbuch der Mathematik,* Verlag H. Deutsch, Thun u. Frankfurt a. M.

Chave, A.D. & Smith, J.T., 1994. On electric and magnetic galvanic distortion tensor decompositions, *J. geophys. Res.,* **99** B3, 4669–4682.

Groom, R.W. & Bailey, R.C., 1989. Decomposition of magnetotelluric impedance tensors in the presence of local three-dimensional galvanic distortion, *J. geophys. Res.,* **94,** 1913–1925.

Groom, R.W. & Bailey, R.C., 1991. Analytic investigation of the effects of near-surface 3D galvanic scatterers on MT tensor decomposition, *Geophysics,* **56,** 496–518.

Harinarayana, T., Hutton, V.R.S. & Jones, P.C., 1993. Lateral variations of conductivity structure across Southern Scotland and Northern England, *Phys. Earth planet. Inter.,* **81,** 25–41.

Hobbs, B.A., 1992. Terminology and symbols for use in studies of electromagnetic induction in the Earth, *Surv. Geophys.,* **13,** 489–515.

Jones, A.G., 1983. The problem of current channelling: a critical review, *Geophys. Surv.,* **6,** 79–122.

Junge, A., 1995. Magnetotellurics in the long period range, *Final Report to the EEC,* Contract ERBCHBICT 93 0610.

Leeder, M.R., 1982. Upper Palaeozoic basins in the British Isles–Caledonide inheritance versus Hercynian plate margin processes, *J. geol. Soc. Lond.,* **139,** 479–491.

Livelybrooks, D.W., Banks, R.J., Parr, R.S. & Hutton, V.R.S., 1993. Inversion of electromagnetic induction data for the Iapetus Suture Zone in the UK, *Phys. Earth planet. Inter.,* **81,** 67–84.

Ritter, O. & Dawes, G.J.K., 1992. A transputer-based multi-station multitechnique geophysical data acquisition system—S.P.A.M. Mk III, *Protokoll über das 14. Koll, Elektromagnetische Tiefenforschung,* pp. 423–435, eds Haak, V. & Rodemann, H., Borkheide.

Ritter, O., Junge, A. & Dawes, G.J.K., 1998. New equipment and processing for magnetotelluric remote reference observations, *Geophys. J. Int.,* **132,** 535–548.

Ritter, P., 1996. Separation of local and regional information in geomagnetic response functions using hypothetical event analysis, *PhD thesis,* University of Edinburgh.

Ritter, P. & Ritter, O., 1997. The bc87 dataset: application of hypothetical event analysis on distorted GDS response functions and some thinsheet modelling studies of the deep crustal conductor, *J. Geomag. Geoelectr.,* **49,** 757–766.

Smith, J.T., 1997. Estimating galvanic-distortion magnetic fields in magnetotellurics, *Geophys. J. Int.,* **130,** 65–72.

Sule, P.O., Hutton, V.R.S. & Dumitrescu, C., 1993. Subsurface structure of SE Scotland from broadband magnetotelluric measurements, *Phys. Earth planet. Inter.,* **81,** 9–24.

Zhang, P., Roberts, R.G. & Pedersen, L.B., 1987. Magnetotelluric strike rules, *Geophysics,* **51,** 267–278.

Zhang, P., Pedersen, L.B., Mareschal, M. & Chouteau, M., 1993. Channelling contribution to tipper vectors: a magnetic equivalent to electrical distortion, *Geophys. J. Int.,* **113,** 693–700.

Zhang, P., Chouteau, M., Mareschal, M., Kurtz, R. & Hubert, C., 1995. High-frequency magnetotelluric investigation of crustal structure in north-central Abitibi, Quebec, Canada, *Geophys. J. Int.,* **120,** 406–418.